1 **Tumour mitochondrial DNA mutations drive aerobic glycolysis to enhance**
2 **checkpoint blockade**

3

4 Mahnoor Mahmood[1], Eric Minwei Liu[2], Amy L. Shergold[1], Elisabetta Tolla[1], Jacqueline
5 Tait-Mulder[1], Alejandro Huerta Uribe[1], Engy Shokry[1], Alex L. Young[1], Sergio Lilla[1],
6 Minsoo Kim[2], Tricia Park[2], J.L. Manchon[3], Crístina Rodríguez-Antona[3,4], Rowan C.
7 Walters[5], Roger J. Springett[5], James N. Blaza[5], Sara Zanivan [1,6], David Sumpton[1],
8 Edward W. Roberts[1,6], Ed Reznik*[2,7,8], Payam A. Gammage*[1,6]

9

10 [1] Cancer Research UK Beatson Institute, Glasgow, UK
11 [2] Computational Oncology Service, Memorial Sloan Kettering Cancer Center, New
12 York, NY, USA
13 [3] Centro Nacional de Investigaciones Oncológicas(CNIO), Madrid, Spain
14 [4] Centro de Investigación Biomédica en Red de Enfermedades Raras CIBERER,
15 Madrid, Spain
16 [5] Structural Biology Laboratory and York Biomedical Research Institute, Department
17 of Chemistry, The University of York, York, UK
18 [6] School of Cancer Sciences, University of Glasgow, UK
19 [7] Marie-Josée and Henry R. Kravis Center for Molecular Oncology, Memorial Sloan
20 Kettering Cancer Center, New York, NY, USA
21 [8] Urology Service, Memorial Sloan Kettering Cancer Center, New York, NY, USA

22

23

24

25 *correspondence to: reznike@mskcc.org or p.gammage@beatson.gla.ac.uk

26

Summary

The mitochondrial genome encodes essential machinery for respiration and metabolic homeostasis but is paradoxically among the most common targets of somatic mutation in the cancer genome, with truncating mutations in respiratory complex I genes being most over-represented[1]. While mitochondrial DNA (mtDNA) mutations have been associated with both improved and worsened prognoses in several tumour lineages[1–3], whether these mutations are drivers or exert any functional effect on tumour biology remains controversial. Here we discovered that complex I-encoding mtDNA mutations are sufficient to remodel the tumour immune landscape and therapeutic resistance to immune checkpoint blockade. Using mtDNA base editing technology[4] we engineered recurrent truncating mutations in the mtDNA-encoded complex I gene, *Mt-Nd5*, into murine models of melanoma. Mechanistically, these mutations promoted utilisation of pyruvate as a terminal electron acceptor and increased glycolytic flux without major effects on oxygen consumption, driven by an over-reduced NAD pool and NADH shuttling between GAPDH and MDH1, mediating a Warburg-like metabolic shift. In turn, without modifying tumour growth, this altered cancer cell-intrinsic metabolism reshaped the tumour microenvironment in both mice and humans, promoting an anti-tumour immune response characterised by loss of resident neutrophils. This subsequently sensitised tumours bearing high mtDNA mutant heteroplasmy to immune checkpoint blockade, with phenocopy of key metabolic changes being sufficient to mediate this effect. Strikingly, patient lesions bearing >50% mtDNA mutation heteroplasmy also demonstrated a >2.5-fold improved response rate to checkpoint inhibitor blockade. Taken together these data nominate mtDNA mutations as functional regulators of cancer metabolism and tumour biology, with potential for therapeutic exploitation and treatment stratification.

Main

It has been known for several decades that >50% of cancers bear somatic mutations of mtDNA[5]. The impact of mtDNA mutations in the germline, the most common cause of inherited metabolic disease in humans[6], is well-established. However, the biological and clinical relevance of mtDNA mutations in cancer remains contentious[5]. Recent efforts have yielded evidence for recurrence and selection of mtDNA mutations in

60   cancer[1], however the majority of variants observed somatically have not been

61   detected in human disease or studied in the germline, thus requiring further study[1,7].

62   Hotspot truncating mutations in mitochondrial complex I genes are a common

63   feature of several cancers, with truncating mutations in complex I (*MT-ND5* in

64   particular) being over-represented compared with mutations in genes encoding

65   respiratory complexes III, IV and V[1]. As complex I is a major site of NADH oxidation[8]

66   we reasoned that the proximal impact of complex I truncating mutations would be loss

67   of NADH : ubiquinone oxidoreductase activity, resulting in redox imbalance with broad

68   downstream impacts on cell metabolism. To test this hypothesis we designed

69   mitochondria-targeted base editors[4] to induce premature stop codons at tryptophan

70   (TGA) codons within mouse *mt-Nd5*, analogous to hotspot mutations found in the

71   human *MT-ND5* gene in tumours[1] (**Figure 1A-C**).

72   TALE-DdCBE G1397/G1333 candidates, bearing nuclear export signals,

73   targeting m.12,436G>A and m.11,944G>A sites were synthesised and screened in

74   mouse B78-D14 amelanotic melanoma cells (B.16 derivative, Cdkn2a null)[9] to identify

75   efficient pairs (**Figure 1D**). Expression of functional pairs (**Extended Data Figure 1A**)

76   resulted in isogenic cell populations bearing ~40% or ~60% mutation heteroplasmy of

77   m.12,436 G>A or m.11,944 G>A truncating mutations following either a single

78   transfection or four consecutive transfections (referred to as m.12,436$^{40\%}$,

79   m.12,436$^{60\%}$, m.11,944$^{40\%}$ and m.11,944$^{60\%}$ respectively) (**Figure 1E**) with limited off-

80   target mutation (**Extended Data Figure 1B**). The resulting stable, isogenic cell lines

81   demonstrated a heteroplasmy-dependent decrease in expression of complex I subunit

82   Ndufb8 without impact on other respiratory chain components (**Figure 1F**). This was

83   supported by Tandem Mass Tagging (TMT)-based mass spectrometry proteomics

84   (**Extended Data Figure 2**) and blue native PAGE analysis of the m.12,436$^{60\%}$ and

85   m.11,944$^{60\%}$ cell lines (**Figure 1G**), confirming that individual complex I subunit

86   abundance, in addition to the proportion of fully assembled complex I, is decreased

87   without substantial impact on other components of the OXPHOS system. In-gel activity

88   assays of complex I and complex II activity further support this finding (**Figure 1G**).

89   mtDNA copy number was not impacted by mutation incidence or heteroplasmy level

90   (**Figure 1H**) and *mt-Nd5* transcript level was unchanged in m.12,436$^{60\%}$ and

91   m.11,944$^{60\%}$ mutant cells compared with controls, consistent with lack of nonsense-

92   mediated decay in mammalian mitochondria (**Extended Data Figure 3A**).

93   Interestingly, none of the heteroplasmic cells exhibited significant decreases in oxygen

94   consumption (**Figure 1I**), adenylate energy charge state (**Figure 1J**) or cell

95   proliferation (**Figure 1K**). However, a ~10mV decrease in the electrical component of

96   the mitochondrial proton motive force , Δ^{Ψ}, coupled to a commensurate trend towards

97   ~10mV increases in the chemical component , ΔpH, resulting in an unchanged total

98   protonmotive force, ΔP, was detected (**Extended Data Figure 3B**). The NAD+ : NADH

99   ratio was significantly impacted in mutant cells (**Figure 1L**), which was also reflected

100   in reduced : oxidised glutathione (GSH : GSSG) ratios (**Extended Data Figure 3C**).

101   The effect on cellular redox poise was further determined in m.12,436[60%] and

102   m.11,944[60%] cells using NAD(P)H fluorescence (**Extended Data Figure 3D**). Taken

103   together, these data demonstrate that truncating mutations in *mt-Nd5* exert

104   heteroplasmy-dependent effects on the abundance of complex I. In turn, partial loss

105   of complex I disrupts cellular redox balance, without significantly impacting cellular

106   energy homeostasis, oxygen consumption or proliferation.

107   Unlabelled metabolomic measurements from m.12,436[60%] and m.11,944[60%]

108   cells revealed consistent differences in metabolite abundance in these cells relative to

109   control (**Extended Data Figure 4**), with notable increases in the steady-state

110   abundance of malate, lactate, fumarate, argininosuccinate (AS) and the metabolically

111   terminal fumarate adducts succinylcysteine and succinicGSH (**Figure 2A**).

112   Heteroplasmy-dependent increases in abundance of lactate and malate in the context

113   of constant succinate in mutant cells suggested that the flow of electrons into

114   mitochondria through the malate-aspartate shuttle (MAS) might be impacted by

115   changes to the redox state of the cell. To study this we first measured the contributions

116   of glutamine-derived carbon to tricarboxylic acid (TCA) cycle metabolites using U-[13]C-

117   glutamine isotope tracing (**Extended Data Figure 5A)**. This indicated increased

118   abundance of malate from cytosolic oxaloacetate (OAA), derived from citrate via ATP

119   citrate lyase, as determined by the abundance of malate m+3 and the ratio of malate

120   m+3 : m+2, which demonstrated a significant, heteroplasmy-dependent increase

121   relative to control (**Extended Data Figure 5B, C**), with a similar pattern of m+3 : m+2

122   labelling observed for urea cycle metabolite AS (**Extended Data Figure 5D**). We then

123   traced the metabolic fate of carbon from 1-^{13}C-glutamine, which exclusively labels

124   metabolites derived from reductive carboxylation (RC) of glutamine (**Figure 2B,**

125   **Extended Data Figure 6A).** This revealed that the increased abundance of malate

126   m+1 occurred at the level of MDH1 (**Figure 2C**), but was not apparent in downstream

127   or upstream metabolites aconitate and aspartate (**Extended Data Figure 6B, C**), with

128   the m+1 labelling pattern of AS again matching that of malate (**Extended Data Figure**

129   **6D**). The increased abundance of malate m+1 and AS +1 was sensitive to siRNA

130   mediated depletion of *Mdh1* but not expression of cytosolically targeted *Lb*NOX

131   (cyto*Lb*NOX), a water-forming NADH oxidase[10] (**Figure 2C, Extended Data Figure**

132   **6E-G**), indicating that increases in malate abundance occur at least partially in the

133   cytosol via MDH1, but are not directly due to gross alteration in cytosolic NAD+ : NADH

134   redox poise.

135   Elevated cellular and extracellular lactate, alongside increased abundance of

136   several glycolytic intermediates (**Figure 2D**) suggested utilisation of pyruvate as an

137   electron acceptor to rebalance NAD+ : NADH via lactate dehydrogenase (LDH). Using

138   U-^{13}C-glucose tracing (**Figure 2E**) we observed increased abundance of lactate m+3

139   in m.12,436$^{60\%}$ and m.11,944$^{60\%}$ cells that was abolished by cyto*Lb*NOX expression

140   (**Figure 2F, Extended Data Figure 7A**). The increase in lactate m+3 did not alter

141   pyruvate m+3 levels (**Extended Data Figure 7B**), or the entry of glucose-derived

142   carbon into the TCA cycle via pyruvate dehydrogenase (PDH) determined by the ratio

143   of citrate m+2 : pyruvate m+3 (**Extended Data Figure 7C**). However, the fate of

144   carbon entering the TCA cycle via pyruvate carboxylase (PC) was substantially

145   altered, with a malate m+3 : citrate m+3 ratio indicative of MDH2 reversal (**Extended**

146   **Data Figure 7D**). Coupling of the MAS with glycolysis is a topic of recent interest, with

147   several reports linking mitochondrial dysfunction with NADH shuttling between

148   GAPDH and MDH1/LDH[11,12]. Using 4-^{2}H$_1$-glucose isotope tracing (**Figure 2G**) we

149   observed an increase in abundance of malate m+1 in m.12,436$^{60\%}$ and m.11,944$^{60\%}$

150   cells, with a similar trend in lactate m+1 abundance, that was sensitive to mito*Lb*NOX

151   treatment and siRNA mediated depletion of *Mdh1* (**Figure 2H, Extended Data Figure**

152   **8A, B**), supporting the notion that the NAD+ : NADH imbalance resulting from partial

153   loss of complex I supports enhanced glycolytic flux by coupling cytosolic components

154   of the MAS with glycolysis. In turn, this increased glycolytic flux rendered m.12,436$^{60\%}$

155   (IC$_{50}$= 0.81mM ±0.064mM) and m.11,944$^{60\%}$ cells (IC$_{50}$= 1.04mM ±0.040mM) more

156   sensitive to the competitive phosphoglucoisomerase inhibitor 2-deoxyglucose (2-DG)

157   compared with wild-type cells (IC$_{50}$= 1.62mM ±0.063mM) (**Figure 2I**), a sensitivity that

158   was further enhanced in a m.12,436$^{80\%}$ model (IC$_{50}$= 0.46mM ±0.080mM).

159   m.12,436$^{60\%}$, m.12,436$^{80\%}$ and m.11,944$^{60\%}$ cells also demonstrated enhanced

160   sensitivity to the low affinity complex I inhibitor metformin relative to wild-type

161   (**Extended Data Figure 9A**). The 60% mutants were not differentially sensitive to

162 potent complex I inhibitor rotenone, although interestingly the m.12,436[80%]
163 demonstrated resistance compared to wild type (**Extended Data Figure 9B**). None of
164 the mutants demonstrated differential sensitivity to complex V inhibitor, oligomycin
165 (**Extended Data Figure 9C**). Taken together, these data demonstrate that truncating
166 mutations in *mt-Nd5* of complex I induce a Warburg-like metabolic state through redox
167 imbalance, not energetic crisis. This influences both cytosolic and mitochondrial
168 components of the MAS, increasing glycolytic flux, enhancing sensitivity to inhibition
169 of this adaptive metabolic strategy and producing elevated levels of characteristic
170 terminal fumarate adducts succinicGSH and succinylcysteine.

171 Having established specific changes in redox metabolism driven by truncating
172 mutations in complex I, we next sought to determine the impact of these metabolic
173 alterations in tumour biology. Syngeneic allografts of m.11,944 G>A cells, m.12,436
174 G>A cells and wild-type controls were performed subcutaneously in
175 immunocompetent C57/Bl6 mice, establishing tumours in 100% of engraftments. All
176 tumours grew at a rate that reached similar humane endpoints (**Figure 3A**) with similar
177 weights and macroscopic histological features (**Figure 3B, Extended Data Figure
178 10A-C**). Bulk measurements of tumour heteroplasmy revealed a subtle, comparable
179 decrease in heteroplasmy of ~10% between engrafted cells and resulting tumours,
180 likely reflecting stroma and immune cell infiltrate (**Extended Data Figure 10D**), with
181 no consistent change in mtDNA copy number detected at bulk level (**Extended Data
182 Figure 10E**). Measurements of metabolites from m.11,944[60%] mutant and control
183 tumours revealed elevated abundance of terminal fumarate adducts succinicGSH and
184 succinylcysteine, characteristic of the metabolic rewiring observed *in vitro* (**Extended
185 Data Figure 10F**). These markers of a consistently altered tumour metabolic profile
186 were coupled to divergent transcriptional signatures between control and mutant
187 tumours (**Figure 3C**), with several signatures of altered immune infiltrate and
188 signalling being significantly elevated in mutant tumours compared with controls,
189 notably allograft rejection, interferon gamma (Ifng) and interferon alpha (Ifna)
190 responses. Higher heteroplasmies correlated to increased signal in the same gene
191 sets (**Extended Data Figure 11**) suggesting a heteroplasmy dose-dependent anti-
192 tumour immune response. To benchmark these findings against human data, we took
193 the Hartwig Medical Foundation (HMF) metastatic melanoma cohort and stratified this
194 by pathogenic mtDNA mutation status into wild-type and >50% variant allele frequency
195 (VAF) groups (see **Methods**). This yielded a set of 355 tumour samples (272 wildtype,

196   83 >50% VAF), with 233 having transcriptional profiles. GSEA analysis revealed
197   consistent transcriptional phenotypes between patient tumours bearing high
198   heteroplasmy pathogenic mtDNA mutations and those identified in our model systems
199   (**Figure 3D**), supporting the observation. To further dissect these effects we employed
200   whole tumour single cell RNA sequencing (scRNAseq) across seven control, three
201   m.12,436$^{60\%}$, three m.11,944$^{60\%}$ and three m.12,436$^{80\%}$ tumours, resulting in 163,343
202   single cell transcriptomes. Cells were clustered using Seurat and cellRanger, with
203   preliminary cell ID determined by scType (see **Methods**) (**Figure 3E,F**). Malignant
204   cells were assigned on the basis of: i) low or nil *Ptprc* (CD45) expression; ii) high
205   epithelial score[13]; iii) aneuploidy determined by copykat analysis[14] (**Extended Data**
206   **Figure 12**). Consistent with bulk tumour transcriptional profiles, GSEA in malignant
207   cells revealed increased Ifna and Ifng signatures coupled to decreased glycolysis
208   signatures in high heteroplasmy tumours (**Figure 3G**), which is not observed *in vitro*
209   prior to implantation (**Extended Data Figure 13**). Downstream regulation of primary
210   metabolic and subsequent immune signalling on malignant cells are also reflected in
211   altered nutrient sensing by mTORC1, transcriptional control of metabolic genes by
212   myc, and TNFa signalling (**Figure 3G)**. GSEA in non-malignant cell clusters revealed
213   similar tumour-wide changes in transcriptional phenotype, with increased Ifna, Ifng,
214   inflammatory response and IL2-Stat5 signalling again observed (**Figure 3H-K**). These
215   indicators of a broad anti-tumour immune response were accompanied by decreased
216   neutrophil residency (**Figure 3L**) and altered monocyte maturation (**Extended Data**
217   **Figure 14A, B)**, with a switch in neutrophil metabolic state indicated by increased
218   OXPHOS gene expression (**Figure 3M**). Further genesets typical of an augmented
219   anti-tumour response, such as allograft rejection, were also elevated alongside a
220   biphasic trend in proportions of tumour resident natural killer and CD4+ T cells
221   (**Extended Data Figure 14C-E**). Taken together these data demonstrate that, in a
222   heteroplasmy-dependent fashion, *mt-Nd5* mutation is sufficient to remodel the tumour
223   microenvironment (TME) and promote an anti-tumour immune response.

224   Treatment of malignant melanoma can include immune checkpoint blockade
225   (ICB) with monoclonal antibodies (mAbs) against T and B-cell expressed immune
226   checkpoint receptor PD1, blocking PD-L1/2 binding to limit tumour-induced immune
227   tolerance. However, the effectiveness of anti-PD1 treatments, and ICB response in
228   melanoma patients more broadly is bimodal, with a substantial proportion of patients
229   not responding to treatment while experiencing a poor morbidity profile. Limited

230   efficacy of ICB has been linked to immunosuppressive tumour-associated neutrophils

231   previously[15] therefore we reasoned that *mt-Nd5* mutant tumours could demonstrate

232   differential sensitivity to ICB, even in an aggressive model of poorly immunogenic

233   melanoma such as B78-D14. Additionally, depleted neutrophil populations in *mt-Nd5*

234   mutant tumours also demonstrated the greatest PD-L1 expression (**Extended Data**

235   **Figure 14F**). To test this we performed further subcutaneous syngeneic allografts of

236   m.12,436$^{40\%}$, m.12,436$^{60\%}$, m.12,436$^{80\%}$, m.11,944$^{40\%}$, m.11,944$^{60\%}$ and wild-type

237   tumours in immunocompetent animals. Tumours grew untreated for 7 days post-graft

238   and animals were dosed with a regimen of intraperitoneal anti-PD1 mAb every 3 days

239   until conclusion of the experiment (**Figure 4A**). A heteroplasmy-defined decrease in

240   tumour weight at endpoint was observed across the mtDNA mutant tumours, with

241   higher mutant heteroplasmies exhibiting greater response to treatment (**Figure 4B,C,**

242   **Extended Figure 15**), consistent with increased sensitivity of mtDNA mutant tumours

243   to immunotherapy. To verify these data we attempted to produce further independent

244   models of aggressive, poorly immunogenic mouse melanoma (**Extended Data Figure**

245   **16A**). This yielded Hcmel12 (Hgf, Cdk4^{R24C})[16] cells engineered to bear >80%

246   m.12,436 G>A mutation, demonstrating consistent cellular and metabolic phenotypes

247   with B78-D14 (**Extended Data Figure 16B-J**). Hcmel12 m.12,436$^{80\%}$ and wild-type

248   Hcmel12 cells were engrafted into mice with a similar experimental workflow as

249   previously (**Figure 4D**). When untreated, Hcmel12 m.12,436^{80} and wild-type tumours

250   demonstrate comparable time to endpoint and tumour weight at endpoint (**Extended**

251   **Data Figure 17A, B**). Changes in bulk heteroplasmy, copy number and tumour

252   metabolism were also similar to those of B78-D14 tumours (**Extended Data Figure**

253   **17C-D).** Moreover, when anti-PD1 treatment was administered, a mtDNA mutation-

254   dependent response was observed in Hcmel12 of similar magnitude to that seen in

255   B78-D14 (**Figure 4 E,F**). To dissect the enhanced ICB response into metabolic v.s.

256   non-metabolic effects of mtDNA mutation, we modified wild-type Hcmel12 cells to

257   constitutively express cyto*Lb*NOX, which reproduces key elements of the cell-

258   extrinsic, mutant *Mt-Nd5*-associated metabolic phenotype, notably glucose uptake

259   and lactate release (**Extended Data Figure 18**). When grafted into mice, Hcmel12

260   cyto*Lb*NOX tumours demonstrated comparable time to endpoint and tumour weight at

261   endpoint as wild-type or *Mt-Nd5* mutant tumours (**Extended Data Figure 17A,B**).

262   When challenged with anti-PD1 treatment, Hcmel cyto*Lb*NOX tumours recapitulate

263   the response of Hcmel *mt-Nd5* m.12,436$^{80\%}$ tumours, indicating that specific changes

264 in redox metabolism associated with mtDNA mutation are sufficient to sensitise the

265 tumour to ICB (**Figure 4E,F**). To benchmark these findings from mice against real

266 world clinical data, we re-analysed a previously reported, well-characterised cohort of

267 majority treatment-naive metastatic melanoma patients given a dosing regimen of the

268 anti-PD1 mAb nivolumab[17]. By identifying mtDNA mutant cancers and stratifying this

269 patient cohort solely on the basis of cancer mtDNA mutation status (**Figure 4G**) the

270 70 patients in this cohort were divided into three groups: mtDNA wild-type (33), <50%

271 VAF (23), and >50% VAF (14). The cancer mtDNA mutation status-naive cohort

272 response rate was 22% for partial or complete responses to nivolumab, however the

273 rate of response for >50% mtDNA mutation VAF cancers was 2.6-fold greater than

274 wild-type or <50% VAF cancer (**Figure 4H**), recapitulating our laboratory findings in

275 patients.

276 These data confirm that somatic mtDNA mutations, commonly observed in

277 human tumours, can exert direct effects on cancer cell metabolic phenotypes. In

278 contrast with clinically presented germline mtDNA mutations,[6] tumour mtDNA

279 mutations are able to exert these effects at a comparably low heteroplasmic burden

280 and without necessarily negatively impacting oxygen consumption or energy

281 homeostasis. The direct link observed between redox perturbations and enhanced

282 glycolytic flux subtly alters our view of mtDNA mutation, to an adaptive gain of function

283 rather than exclusively loss of function event, and the discovery that mtDNA mutations

284 can underpin aerobic glycolysis warrants further assessment of the relationship

285 between classical Warburg metabolism[18] and mtDNA mutation status.

286 Beyond cancer cell intrinsic effects, the data here reveal that a functional

287 consequence of somatic mtDNA mutation in tumour biology is the remodelling of the

288 TME, mediating therapeutic susceptibility to ICB. Truncating mutations to mtDNA,

289 analogous to those described here, affect 10% of all cancers regardless of tissue

290 lineage, with non-truncating, pathogenic mtDNA mutations presenting in a further 40-

291 50% of all cancers. A broad influence over the anti-tumour immune response in these

292 cancers might also be expected.

293 Beyond stratification and exploitation of mtDNA mutant tumour vulnerability,

294 our data suggest that the ICB response-governing effects we observe are principally

295 metabolic in nature. Recreating such a metabolic state in mtDNA wild-type or

296 'immune cold' tumour types could therefore also be of benefit.

297

Methods

Maintenance, transfection and FACS of cell lines

B78 melanoma cells (RRID:CVCL_8341) and Hcmel12 cells[16] were maintained in DMEM containing GLUTAMAX[TM], 0.11g/L sodium pyruvate, 4.5g/L D-glucose (Life Technologies) and supplemented with 1% penicillin/ streptomycin (P/S) (Life Technologies) and 10% FBS (Life Technologies). Cells were grown in incubators at 37°C and 5% CO_2. Cells were transfected using Lipofectamine 3000 (Life Technologies) using a ratio of 5μg DNA : 7.5μl Lipofectamine 3000. Cells were sorted as outlined in[19] and thereafter grown in the same base DMEM media supplemented with 20% FBS and 100μg/mL of uridine (Sigma).

Use of animal models

Animal experiments were carried out in accordance with the UK Animals (Scientific Procedures) Act 1986 (P72BA642F) and by adhering to the ARRIVE guidelines with approval from the local Animal Welfare and Ethical Review Board of the University of Glasgow. Mice were housed in conventional cages in an animal room at a controlled temperature (19–23 °C) and humidity (55 ± 10%) under a 12hr light/dark cycle. Experiments only used male C57BL/6 mice at ~8 weeks of age which were injected subcutaneously with either 2.5×10^5 B78 cells or 1×10^4 HcMel12 cells, both prepared in 1:1 RPMI (Life Technologies) and Matrigel (Merck). Mice were culled at an endpoint of 15mm tumour measurement.

For immunotherapy experiments, mice were put on a dosing regimen of 200μg of anti-PD1 given intraperitoneally twice a week. The first dose was given 7 days post-injection and all mice were sacrificed at 21 or 13 days post-injection for B78 or HcMel12 cells respectively.

Construction of DdCBE plasmids

TALEs targeting mt.12,436 and mt.11,944 were designed with advice from Beverly Mok and David Liu (Broad Institute, USA). TALEs were synthesised (ThermoFisher GeneArt) as illustrated in Figure 1A with the left TALEs being cloned into pcDNA3.1(-)_mCherry[19] and the right into pTracer CMV/Bsd[19], allowing for the co-expression of mCherry and GFP respectively.

332

333

334 Pyrosequencing assay

335 DNA was extracted from cell pellets using the DNeasy Blood & Tissue Kit (Qiagen) as

336 per the manufacturer's instructions. PCR was then performed using the PyroMark

337 PCR Mix (Qiagen) for 50 cycles with an annealing temperature of 50°C and an

338 extension time of 30sec. PCR products were run on the PyroMark Q48 Autoprep

339 (Qiagen) as per the manufacturer's instructions.

340

341 PCR primers for mt.12,436

342 Forward: 5'-ATATTCTCCAACAACAACG-3'

343 Reverse: 5'-**biotin**-GTTATTATTAGTCGTGAGG-3'

344

345 PCR primers for mt.11,944

346 Forward: 5'-CTTCATTATTAGCCTCTTAC-3'

347 Reverse: 5'-**biotin**-GTCTGAGTGTATATCATG-3'

348

349 Sequencing primer for mt.12,436

350 5'-TTGGCCTCCACCCAT-3'

351

352 Sequencing primer for mt.11,944

353 5'-TAATTACAACCTGGCACT-3'

354

355 Protein extraction and measurement

356 Cell pellets were lysed in RIPA buffer (Life Technologies) supplemented with

357 cOmplete Mini Tablets and cOmplete Mini Protease Inhibitor Tablets (Roche).

358 Samples were incubated on ice for 20mins and then spun at 14,000g for 20mins. The

359 isolated supernatant containing total cellular protein was then quantified using a DC

360 Protein Assay (Bio-Rad Laboratories) performed as per the manufacturer's

361 instructions.

362

363 Immunoblotting

364 To detect protein via western blotting 60µg of protein was resolved on SDS-PAGE 4-

365 12% Bis-Tris Bolt gels (Life Technologies). Protein was transferred onto a

366 nitrocellulose membrane using a Mini Trans-Bolt Cell (Bio-Rad Laboratories).

367 Membranes were then stained with Ponceau S Staining Solution (Life Technologies)

368 to measure loading before overnight incubation with the primary antibody prepared in

369 5% milk in 1X TBST. Imaging was performed using the Odyssey DLx Imaging system

370 (Licor).

371 Antibodies:

372 Total OXPHOS Rodent WB Antibody Cocktail (1:800, ab110413, Abcam)

373 Monoclonal Anti-FLAG® M2 antibody (1:1000, F1804, Sigma)

374 Recombinant anti-vinculin antibody (1:10,000, ab129002, Abcam)

375

376 <u>Mitochondrial Isolation</u>

377 Cells were grown in Falcon Cell Culture 5-layer flasks (Scientific Laboratory Supplies)

378 and grown to near 100% confluency. Cells were then harvested and mitochondria

379 were extracted as described in [20].

380

381 <u>Blue-Native PAGE</u>

382 Isolated mitochondria were solubilized in 1X NativePage Sample Buffer supplemented

383 with 1% Digitonin (Life Technologies). Samples were incubated on ice for 10min and

384 then centrifuged at 20,000g for 30min at 4°C. Supernatants were isolated and total

385 extracted protein quantified using the DC Protein Assay (Bio-Rad Laboratories).

386 Samples were prepared and run on NativePage 4-12% Bis-Tris gels as per the

387 manufacturer's instructions (Life Technologies). For immunoblotting, samples were

388 transferred onto PVDF membranes using Mini Trans-Bolt Cell (Bio-Rad Laboratories).

389 Subsequent probing and imaging was performed as described above for

390 immunoblotting. Loading was visualised using Coomassie Blue on a duplicate gel.

391 In-gel assays were performed for complex I and II activity as described in [20].

392

393 <u>Digital droplet PCR</u>

394 mt-Nd5 primers

395 Forward: 5'-TGCCTAGTAATCGGAAGCCTCGC-3'

396 Reverse: 5'-TCAGGCGTTGGTGTTGCAGG-3'

397

398 VDAC1 primers

399 Forward: 5'-CTCCCACATACGCCGATCTT-3'

400   Reverse: 5'-GCCGTAGCCCTTGGTGAAG-3'

401

402   Samples were prepared in triplicate in a 96-well plate using 1ng of DNA, 100nM of

403   each primer, 10µL of QX200 ddPCR EvaGreen Supermix and water to 20µL. Droplet

404   generation, PCR and measurements were then performed on the QX200 Droplet

405   Digital PCR System (Bio-Rad Laboratories) as per the manufacturer's instructions with

406   the primer annealing temperature set at 60°C.

407

408   <u>Seahorse Assay</u>

409   The Seahorse XF Cell Mito Stress Test (Agilent) was performed as per the

410   manufacturer's instructions. Briefly, cells were plated into a Seahorse 96-well plate at

411   2×10^4 cells/well a day prior to the assay. A sensor cartridge was also allowed to

412   hydrate in water at 37°C overnight. The water was replaced with Seahorse XF

413   Calibrant and the sensor cartridge was re-incubated for 45mins. Oligomycin, FCCP,

414   Rotenone and Antimycin A were then added to their respective seahorse ports to a

415   final concentration of 1µM in the well before sensor calibration on the Seahorse XFe96

416   Analyser (Agilent). Meanwhile, cell media was replaced with 150µL Seahorse XF

417   Media supplemented with 1% FBS, 25mM glucose, 1mM sodium pyruvate and 2mM

418   glutamine and incubated at 37°C for 30mins. The cell plate was then inserted into the

419   analyser post-calibration and run.

420   For read normalisation, protein extraction and measurement was performed as

421   described above.

422

423   <u>In vitro metabolomics</u>

424   Cells were seeded two days prior to metabolite extraction to achieve 70-80%

425   confluency on the day of extraction. Plates were incubated at 37°C and 5% CO_2

426   overnight. The following day, cells were replenished with excess fresh media to

427   prevent starvation at the point of extraction. For steady-state experiments, media was

428   prepared as described above with the substitution of GLUTAMAX™ with 2mM L-

429   glutamine. For U-^{13}C-glucose and 4-^{2}H$_1$-glucose isotope tracing experiments, media

430   was prepared as follows: DMEM, no glucose (Life Technologies) supplemented with

431   0.11g/L sodium pyruvate, 2mM L-glutamine, 20% FBS, 100µg/mL uridine and 25mM

432   glucose isotope (Cambridge Isotopes). For isotope tracing experiments using U-^{13}C-

433   glutamine and 1-^{13}C-glutamine, DMEM containing 4.5g/L D-glucose and 0.11g/L

434 sodium pyruvate was supplemented with 20% FBS, 100µg/mL uridine and 4mM

435 glutamine isotope (Cambridge Isotopes).

436 On the day of extraction, 20µL of media was added to 980µL of extraction buffer from

437 each well. Cells were then washed twice with ice-cold PBS. Extraction buffer

438 (50:30:20, v/v/v, methanol/acetonitrile/water) was then added to each well (600µL per

439 2 x10^6) and incubated for 5min at 4°C. Samples were centrifuged at 16,000g for

440 10mins at 4°C and the supernatant was transferred to liquid chromatography-mass

441 spectrometry (LC-MS) glass vials and stored at -80°C until run on the mass

442 spectrometer.

443 Mass spectrometry and subsequent targeted metabolomics analysis was performed

444 as described in [21]. Compound peak areas were normalised using the total measured

445 protein per well quantified with a modified Lzowry assay[21].

446

447 <u>In vitro measurements of fumarate</u>

448 <u>Samples were prepared as described above.</u>

449 Fumarate analysis was carried out using a Q Exactive Orbitrap mass spectrometer

450 (Thermo Scientific) coupled to an Ultimate 3000 HPLC system (Themo Fisher

451 Scientific). Metabolite separation was done using a HILIC-Z column (InfinityLab

452 Poroshell 120, 150 x 2.1 mm, 2.7µm, Agilent) with a mobile phase consisting of a

453 mixture of A (40mM ammonium formate pH=3) and B (90% ACN / 10% 40 mM

454 ammonium formate). The flow rate was set to 200 µL/min and the injection volume

455 was 5 µL. The gradient started at 10% A for 2 min, followed by a linear increase to

456 90% A for 15 min; 90% A was then kept for 2 minutes, followed by a linear decrease

457 to 10% A for 2 min and a final re-equilibration step with 10% A for 5 min. The total

458 run time was 25 min. The Q Exactive mass spectrometer was operated in negative

459 mode with a resolution of 70,000 at 200 m/z across a range of 100 to 150 m/z

460 (automatic gain control (AGC) target of 1x10^6 and maximum injection time (IT) of 250

461 ms).

462

463

464 <u>siRNA knockdown for metabolomics</u>

465 1.2 x 12^4 cells were plated into 12-well cell culture plates and incubated at 37°C and

466 5% CO$_2$ overnight. The following day, cells were transfected with 5µL of 5µM siRNA

467 with 5µL of DharmaFECT 1 Transfection Reagent (Horizon Discovery). Cells were

468   either transfected with ON-TARGETplus MDH1 siRNA (L-051206-01-0005, Horizon

469   Discovery) or ON-TARGETplus non-targeting control siRNA (D-001810-10-05,

470   Horizon Discovery). Cells were supplemented with excess media the following day

471   and metabolites extracted 48hrs post-transfection as outlined above.

472

473   <u>LbNOX treatment for metabolomics</u>

474   pUC57-LbNOX (addgene #75285) and pUC57-mitoLbNOX (addgene #74448) were

475   gifts from Vamsi Mootha. Both enzyme sequences were amplified using Phusion PCR

476   (Life Technologies) as per the manufacturer's instructions. These products were

477   cloned into pcDNA3.1(-)_mCherry[19] via the *NheI* and *BamHI* restriction sites and used

478   for subsequent experiments.

479   Forward for LbNOX: 5'-GGTGGTGCTAGCCGCATGAAGGTCACCG-3'

480   Forward for mitoLbNOX: 5'-GGTGGTGCTAGCCGCATGCTCGCTACAAG-3'

481   Reverse: 5'-GGTGGTGGATCCTTACTTGTCATCGTCATC-3'

482

483   Cells were transfected and sorted as described above and 3×10^4 mCherry+ cells

484   were plated per well into a 12-well plate. Cells were allowed to recover overnight at

485   37°C and 5% CO_2 followed by the addition of excess media to each well. Metabolites

486   were extracted the following day and analysed as outlined above.

487

488   <u>Bulk tumour metabolomics</u>

489   Tumour fragments (20-40mg) were flash frozen on dry ice when harvested.

490   Metabolites were extracted using the Precellys Evolution homogenizer (Bertin) with

491   25µL of extraction buffer per mg of tissue. Samples were then centrifuged at 16,000g

492   for 10mins at 4°C and the supernatant was transferred to LC-MS glass vials and stored

493   at -80°C until analysis.

494   Samples were run and subsequent targeted metabolomics analysis was performed as

495   described in [21]. Compound peak areas were normalised using the mass of the tissue.

496

497   <u>Calculating cell sensitivity to 2-DG</u>

498   Cells were plated in a 96-well plate at 500 cells/well in 200µL of cell culture media.

499   Plates were incubated overnight at 37°C and 5% CO_2. The following day, media was

500   replaced with 0 – 100mM 2-DG in quadruplicate. Plates were imaged once every 4

501   hrs on the IncuCyte Zoom (Essen Bioscience) for 5 days. Final confluency

502   measurements were calculated using the system algorithm and the IC_{50} was

503   determined by GraphPad Prism.

504

505   Bulk tumour RNAseq

506   Tumour fragments (20-40mg) were stored in RNAlater (Sigma) and stored at -80°C.

507   Samples were sent to GeneWiz Technologies for RNA extraction and sequencing.

508

509   HcMel12 Transduction

510   cytoLbNOX was cloned into the lentiviral plasmid pLex303 via the NheI and BamHI

511   restriction sites and transduction of HcMel12 was performed as described in [22].

512   Transduced cells were selected via supplementation of 8μg/mL blasticidin, and single

513   clones were selected out from the surviving bulk population. cytoLbNOX expression

514   was confirmed using immunoblotting.

515   pLEX303   was   a   gift   from   David   Bryant   (Addgene   plasmid   #162032;

516   http://n2t.net/addgene:162032 ; RRID:Addgene_162032).

517

518   Hartwig Dataset Analysis

519   The Hartwig Medical Foundation (HMF) dataset included WGS data from tumor

520   metastases normal-matched samples from 355 melanoma patients (skin primary

521   tumor location), of whom 233 had additional RNA sequencing data of the tumor

522   samples. mtDNA somatic mutations were called and annotated as previously

523   described[1].In brief, variants called by both Mutect2 and samtools mpileup were

524   retained and merged using vcf2maf, which embeds the Variant Effect Predictor (VEP)

525   variant annotator. Variants within the repeat regions (chrM:302-315, chrM:513-525,

526   and chrM:3105-3109) were filtered out. Next, variants were filtered out if the Variant

527   Allele Fraction (VAF) was lower than 1% in the tumor samples and lower than 0.24%

528   in the normal sample, as previously described (Yuan et al, 2020). Finally, somatic

529   variants were kept when supported by at least one read in both the forward and the

530   reverse orientations. Samples with >50% VAF mtDNA Complex I truncating

531   (frameshift indels, translation start site and nonsense mutations) and missense

532   mutations were classified as mutated and the rest as wild-type. Gene expression data

533   was obtained from the output generated by the isofox pipeline, provided by HMF.

534   Adjusted Transcript per Million ("adjTPM") gene counts per sample were merged into

535   a matrix. Gene expression and mutation data were used to perform differential

536   expression analysis with DESeq2 in R using the DESeqDataSetFromMatrix function.

537   Gene set enrichment analysis (GSEA) was performed with fGSEA in R with a minimum

538   set size of 15 genes, a maximum of 500 genes and 20,000 permutations, against the

539   mSigDB Hallmark gene set collection (v.7.5.1). Normalized Enrichment Score (NES)

540   were ranked for significant upregulated and downregulated gene sets.

541

542   <u>Statistical methods</u>

543   No statistical test was used to determine sample sizes. Mice were randomly assigned

544   to different experimental groups. Samples were blinded to machine operators

545   (metabolomics, proteomics, RNAseq). Researchers were blinded to experimental

546   groups for *in vivo* anti-PD1 experiments. Specific statistical tests used to determine

547   significance, group sizes (*n*) and *P* values are provided in the figure

548   legends. *P* values < 0.05, <0.01 and <0.001 are represented as *, ** and ***

549   respectively in figures. All statistical analysis was carried out using Prism (GraphPad)

550   and Rstudio.

551

552   <u>Data and Code Availability Statement</u>

553   All non-commercial plasmids used have been deposited with addgene (Gammage

554   Lab). All metabolomic data, mtDNA sequencing, bulk and single cell RNAseq and

555   proteomic data contained in this study are available in the supplementary information

556   or via specified public repositories.

557

558   All custom code will be made available via Reznik lab Github.

559

560   **References**

561   1.   Gorelick, A. N. *et al.* Respiratory complex and tissue lineage drive recurrent

562   mutations in tumour mtDNA. *Nat. Metab.* (2021) doi:10.1038/s42255-021-

563   00378-8.

564   2.   Hopkins, J. F. *et al.* Mitochondrial mutations drive prostate cancer aggression.

565   *Nat. Commun.* (2017) doi:10.1038/s41467-017-00377-y.

566   3.   Schöpf, B. *et al.* OXPHOS remodeling in high-grade prostate cancer involves

567   mtDNA mutations and increased succinate oxidation. *Nat. Commun.* **11**,

568   (2020).

569   4.   Mok, B. Y. *et al.* A bacterial cytidine deaminase toxin enables CRISPR-free

570   mitochondrial base editing. *Nature* **583**, 631–637 (2020).

571   5.   Kim, M., Mahmood, M., Reznik, E. & Gammage, P. A. Mitochondrial DNA is a major source of driver mutations in cancer. *Trends in Cancer* **8**, 1046–1059 (2022).

574   6.   Gorman, G. S. *et al.* Mitochondrial diseases. *Nat. Rev. Dis. Prim.* (2016) doi:10.1038/nrdp.2016.80.

576   7.   Yuan, Y. *et al.* Comprehensive molecular characterization of mitochondrial genomes in human cancers. *Nat. Genet.* **52**, 342–352 (2020).

578   8.   Guerrero-Castillo, S. *et al.* The Assembly Pathway of Mitochondrial Respiratory Chain Complex I. *Cell Metab.* (2017) doi:10.1016/j.cmet.2016.09.002.

581   9.   Graf, L. H., Kaplan, P. & Silagi, S. Efficient DNA-mediated transfer of selectable genes and unselected sequences into differentiated and undifferentiated mouse melanoma clones. *Somat. Cell Mol. Genet.* (1984) doi:10.1007/BF01534903.

585   10. Titov, D. V. *et al.* Complementation of mitochondrial electron transport chain by manipulation of the NAD+/NADH ratio. *Science (80-.).* (2016) doi:10.1126/science.aad4017.

588   11. Gaude, E. *et al.* NADH Shuttling Couples Cytosolic Reductive Carboxylation of Glutamine with Glycolysis in Cells with Mitochondrial Dysfunction. *Mol. Cell* **69**, 581-593.e7 (2018).

591   12. Wang, Y. *et al.* Saturation of the mitochondrial NADH shuttles drives aerobic glycolysis in proliferating cells. *Mol. Cell* **82**, 3270-3283.e9 (2022).

593   13. Dong, J. *et al.* Single-cell RNA-seq analysis unveils a prevalent epithelial/mesenchymal hybrid state during mouse organogenesis. *Genome Biol.* (2018) doi:10.1186/s13059-018-1416-2.

596   14. Gao, R. *et al.* Delineating copy number and clonal substructure in human tumors from single-cell transcriptomes. *Nat. Biotechnol.* (2021) doi:10.1038/s41587-020-00795-2.

599   15. Coffelt, S. B., Wellenstein, M. D. & De Visser, K. E. Neutrophils in cancer: Neutral no more. *Nat. Rev. Cancer* **16**, 431–446 (2016).

601   16. Bald, T. *et al.* Ultraviolet-radiation-induced inflammation promotes angiotropism and metastasis in melanoma. *Nature* **507**, 109–113 (2014).

603   17. Riaz, N. *et al.* Tumor and Microenvironment Evolution during Immunotherapy

604   with Nivolumab. *Cell* (2017) doi:10.1016/j.cell.2017.09.028.

605   18. DeBerardinis, R. J. & Chandel, N. S. We need to talk about the Warburg effect.

606   *Nat. Metab.* **2**, 127–129 (2020).

607   19. Gammage, P. A., Van Haute, L. & Minczuk, M. Engineered mtZFNs for

608   manipulation of human mitochondrial DNA heteroplasmy. in *Methods in*

609   *Molecular Biology* vol. 1351 145–162 (Humana Press Inc., 2016).

610   20. Fernandez-Vizarra, E. & Zeviani, M. Blue-Native Electrophoresis to Study the

611   OXPHOS Complexes. in *Methods in Molecular Biology* (2021).

612   doi:10.1007/978-1-0716-0834-0_20.

613   21. Villar, V. H. *et al.* Hepatic glutamine synthetase controls N 5-methylglutamine

614   in homeostasis and cancer. *Nat. Chem. Biol.* (2022) doi:10.1038/s41589-022-

615   01154-9.

616   22. Nacke, M. *et al.* An ARF GTPase module promoting invasion and metastasis

617   through regulating phosphoinositide metabolism. *Nat. Commun.* (2021)

618   doi:10.1038/s41467-021-21847-4.

619   23. Cao, X. *et al.* The mammalian cytosolic thioredoxin reductase pathway acts via

620   a membrane protein to reduce ER-localised proteins. *J. Cell Sci.* **133**, (2020).

621   24. Cox, J. & Mann, M. MaxQuant enables high peptide identification rates,

622   individualized p.p.b.-range mass accuracies and proteome-wide protein

623   quantification. *Nat. Biotechnol.* **26**, (2008).

624   25. Cox, J. *et al.* Andromeda: A peptide search engine integrated into the

625   MaxQuant environment. *J. Proteome Res.* **10**, 1794–1805 (2011).

626   26. Apweiler, R. The Universal Protein Resource (UniProt) in 2010. *Nucleic Acids*

627   *Res.* **38**, (2010).

628   27. Tyanova, S. *et al.* The Perseus computational platform for comprehensive

629   analysis of (prote)omics data. *Nature Methods* (2016)

630   doi:10.1038/nmeth.3901.

631   28. Ritchie, M. E. *et al.* limma powers differential expression analyses for RNA-

632   sequencing and microarray studies. *Nucleic Acids Res.* **43**, e47 (2015).

633   29. Rocha, M. & Springett, R. Measuring the functionality of the mitochondrial

634   pumping complexes with multi-wavelength spectroscopy. *Biochim. Biophys.*

635   *Acta - Bioenerg.* **1860**, 89–101 (2019).

636   30. Kim, N., Ripple, M. O. & Springett, R. Measurement of the mitochondrial

637   membrane potential and pH gradient from the redox poise of the hemes of the

638   bc 1 complex. *Biophys. J.* **102**, 1194–1203 (2012).

639 31. Papalazarou, V., Drew, J., Juin, A., Spence, H. J. & Nixon, C. Collagen-VI

640   expression is negatively mechanosensitive in pancreatic cancer cells and

641   supports the metastatic niche. *J. Cell Sci.* **135**, (2022).

642 32. Zheng, G. X. Y. *et al.* Massively parallel digital transcriptional profiling of single

643   cells. *Nat. Commun. 2017 81* **8**, 1–12 (2017).

644 33. Hao, Y. *et al.* Integrated analysis of multimodal single-cell data. *Cell* **184**,

645   3573-3587.e29 (2021).

646 34. Korsunsky, I. *et al.* Fast, sensitive and accurate integration of single-cell data

647   with Harmony. *Nat. Methods 2019 1612* **16**, 1289–1296 (2019).

648 35. Korsunsky, I., Nathan, A., Millard, N. & Raychaudhuri, S. Presto scales

649   Wilcoxon and auROC analyses to millions of observations. *bioRxiv* 653253

650   (2019).

651 36. Korotkevich, G. & Sukhov, V. Fast gene set enrichment analysis. *bioRxiv* 1–29

652   (2016).

653

654

655

656

657

Acknowledgements

Author contributions

M.M., E.R. and P.A.G. conceived the study. M.M. and P.A.G. designed the experiments. M.M. conducted in vitro and in vivo experiments, analysed data and co-wrote the paper. E.M.L., M.K., T.P. and J.L.M. and E.R. conducted computational analyses. A.S., E.T., A.L.Y. and E.W.R conducted in vivo experiments. J.T.-M.

672   conducted in vitro experiments. A.U., E.S. and D.S. performed metabolomic mass
673   spectrometry. S.L. and S.Z. performed proteomic mass spectrometry and analysis.
674   R.W., R.J.S. and J.N.B performed biophysical experiments. C.R.-A supervised
675   computational analyses. E.R. and P.A.G. supervised the study, obtained funding
676   (CRUK BI Core Funding: A_BICR_1920_Gammage to P.A.G.; ERC Starting Grant via
677   UKRI: EP/X035581/1 to P.A.G.; NIH NCI: 1R37CA276200 to E.R. and P.A.G.) and
678   wrote the paper, with the involvement of all authors.

679

680   **Competing interests**
681   M.M., E.R. and P.A.G. are named inventors on patent applications resulting from this
682   work filed by Cancer Research Horizons. P.A.G is a shareholder, and has been a
683   consultant and Scientific Advisory Board member to Pretzel Therapeutics Inc.

684

685   **Materials & Correspondence**
686   All requests for biological materials, computer code or data should be addressed to
687   p.gammage@beatson.gla.ac.uk and reznike@mskcc.org

688

689   **Figure Legends**

690

691   **Figure 1**. Mitochondrial base editing to produce isogenic cell lines bearing
692   independent truncating mutation heteroplasmies in *mt-Nd5*. **A** Schematic of TALE-
693   DdCBE design employed. TALEs were incorporated into a backbone containing a
694   mitochondria-targeting cassette, split-half DdCBE and uracil glycosylase inhibitor
695   (UGI). **B** Schematic of the murine mtDNA. Targeted sites within *mt-Nd5* are indicated.
696   **C** TALE-DdCBE pairs used to induce a G>A mutation at mt.12,436 and mt.11,944. **D**
697   Workflow used to produce *mt-Nd5* mutant isogenic cell lines. **E** Heteroplasmy
698   measurements of cells generated in D (n = 6 separate wells were sampled). **F**
699   Immunoblot of indicative respiratory chain subunits. Representative result is shown.
700   **G** Assembled complex I abundance and in-gel activity of complexes I and II.
701   Representative result is shown. **H** mtDNA copy number (n= 9 separate wells were
702   sampled). **I** Basal oxygen consumption rate (OCR) (n = 9-12 measurements (12 wells
703   per measurement) were made). **J** Energy (adenylate) charge state (n = 17 separate
704   wells were sampled). **K** Proliferation rate of cell lines in permissive growth media. (n =
705   12 separate wells were measured in three batches) **L** NAD+:NADH ratio (n= 11-12

706   separate wells were measured). All P-values were determined using a one-way

707   ANOVA test with (E, H-I, K) Sidak multiple comparisons test or (J,L) Fisher's LSD Test.

708   Error bars indicate SD. Measure of centrality is mean.

709

710   **Figure 2**: Mutant cells undergo a metabolic shift towards glycolysis due to cellular

711   redox imbalance. **A** Heatmap of unlabelled steady-state abundance of select

712   mitochondrial metabolites, arginine, argininosuccinate (AS) and terminal fumarate

713   adducts succinylcysteine (succ. Cys) and succinicGSH (succ.GSH). **B** Labelling fate

714   of ^{13}C derived from $1\text{-}^{13}C$-glutamine. **C** Malate m+1 abundance, derived from $1\text{-}^{13}C$-

715   glutamine with indicated treatment (n = 6-11 separate wells were sampled). **D**

716   Heatmap of unlabelled steady-state metabolite abundances for select intracellular

717   glycolytic intermediates and extracellular lactate (ex. lactate). **E** Labelling fate of U-

718   ^{13}C-glucose. **F** Abundance of U-^{13}C-glucose derived lactate m+3 with indicated

719   treatment (n = 6-9 separate wells were sampled). **G** Labelling fate of ^{2}H derived from

720    $4\text{-}^{2}H_{1}$-glucose; mitoLbNOX not shown for clarity. **H** Malate m+1 abundance, derived

721   from $4\text{-}^{2}H_{1}$-glucose with indicated treatment (n = 5-16 separate wells were sampled).

722   **I** IC$_{50}$ curves for 2-DG (n = 4 separate wells measured per drug concentration). This

723   was repeated 3 times and a representative result is shown. P-values were determined

724   using a one-way ANOVA test with (A, D) Sidak multiple comparisons test or Fisher's

725   LSD Test (C, F, H). Error bars indicate SD. Measure of centrality is mean.

726

727   **Figure 3**: Tumour mtDNA mutations reshape the immune microenvironment. **A**

728   Survival of C57/BL6 mice subcutaneously injected with indicated cells (n = 5-12

729   animals per condition). **B** Tumour weight at endpoint (n = 5-12 tumours per genotype).

730   **C** Geneset enrichment analysis (GSEA) of bulk tumour RNA sequencing (RNAseq)

731   data (n=5-6 tumours per genotype). Only genesets with adj. P-value <0.1 are shown.

732   **D** GSEA of RNAseq obtained from Hartwig Medical Foundation (HMF) metastatic

733   melanoma patient cohort. Cancers are stratified by mtDNA status into wild-type and

734   mtDNA mutant with >50% variant allele frequency (VAF). **E** UMAP of seurat clustered

735   whole tumour scRNAseq from indicated samples. **F** UMAP indicating cell type IDs.

736   DC, dendritic cells. pDC, plasmacytoid dendritic cell. **G** GSEA of malignant cells

737   identified in scRNAseq analysis. UMAPs coloured by GSEA score for: **H** interferon

738   alpha response; **I** interferon gamma response; **J** inflammatory response; **K** IL2-Stat5

739   signalling. **L** Proportion of tumour resident neutrophils relative to total malignant and

740   non-malignant cells (n = 17 tumours). **M** UMAP coloured by GSEA for OXPHOS

741   geneset. One-way ANOVA test with Sidak multiple comparisons test (B), Wilcoxon

742   signed rank test (G-K) and two-tailed student's t-test (L-O) were applied. Error bars

743   indicate SD (B) or SEM (L-O). Measure of centrality is mean. Box plots indicate

744   interquartile range (J-M). NES: normalised expression score.

745

746   **Figure 4**: mtDNA mutation-associated microenvironment remodelling sensitises

747   tumours to checkpoint blockade. **A** Schematic of the experimental plan and dosing

748   regimen for B78-D14 tumours with anti-PD1 monoclonal antibody (mAb). **B**

749   Representative images of harvested tumours at day 21. **C** Tumour weights at day 21

750   (n = 10-19 tumours per genotype). **D** Schematic of experimental plan and dosing

751   regimen for Hcmel12 tumours with anti-PD1 mAb. **E** Representative images of

752   harvested tumours at day 13. **F** Tumour weights at day 13 (n = 7 tumours per

753   genotype). **G** Stratification of a metastatic melanoma patient cohort by mtDNA status.

754   **H** Response rate of patients to nivolumab by tumour mtDNA mutation status. One-

755   way ANOVA test with Sidak multiple comparisons test (C), student's one-tailed t-test

756   (F)or chi-squared test (H) were applied. Error bars indicate SD. Measure of centrality

757   is mean.

758

Mahmood et al - Figure 1
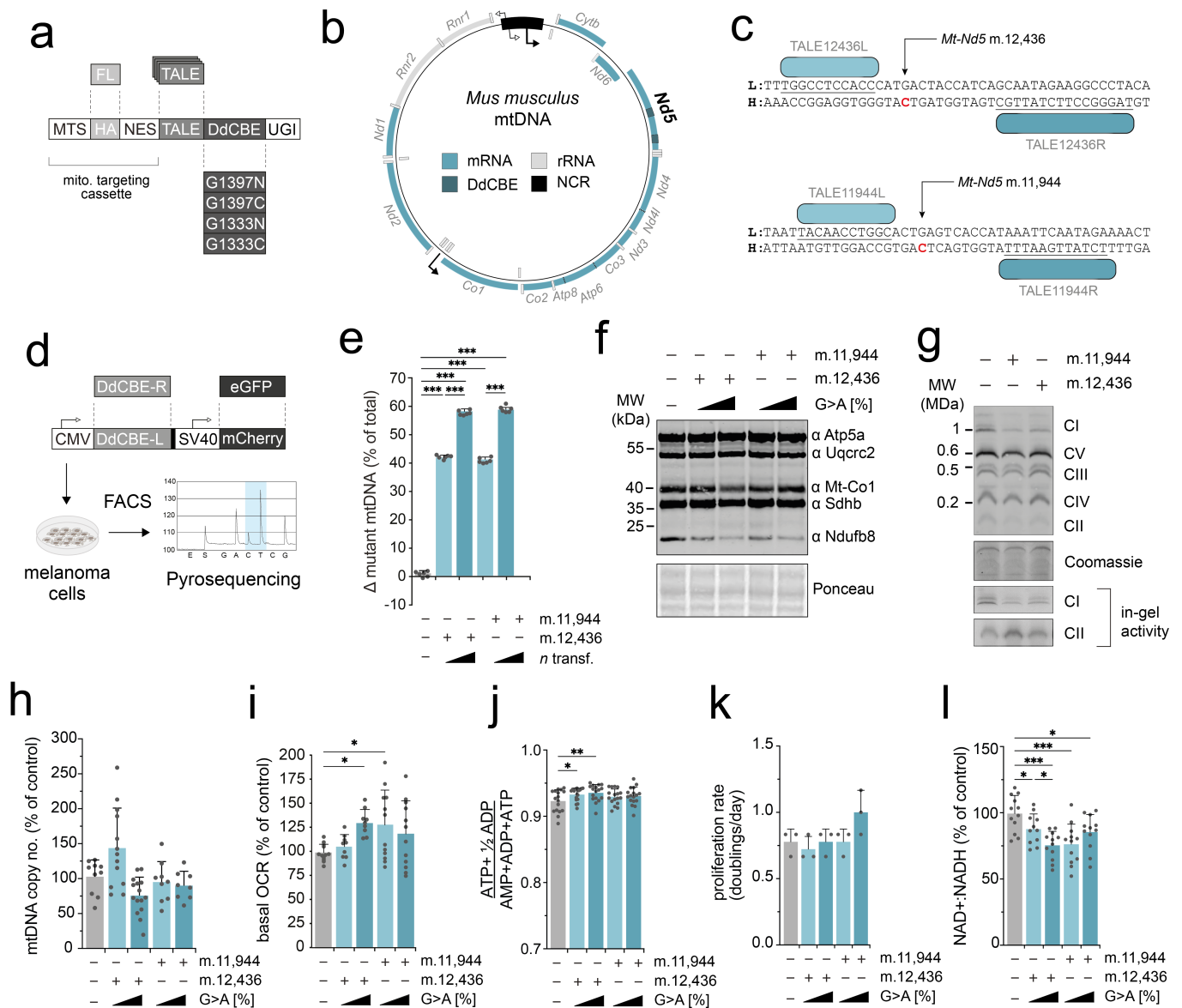
Mahmood et al - Figure 2
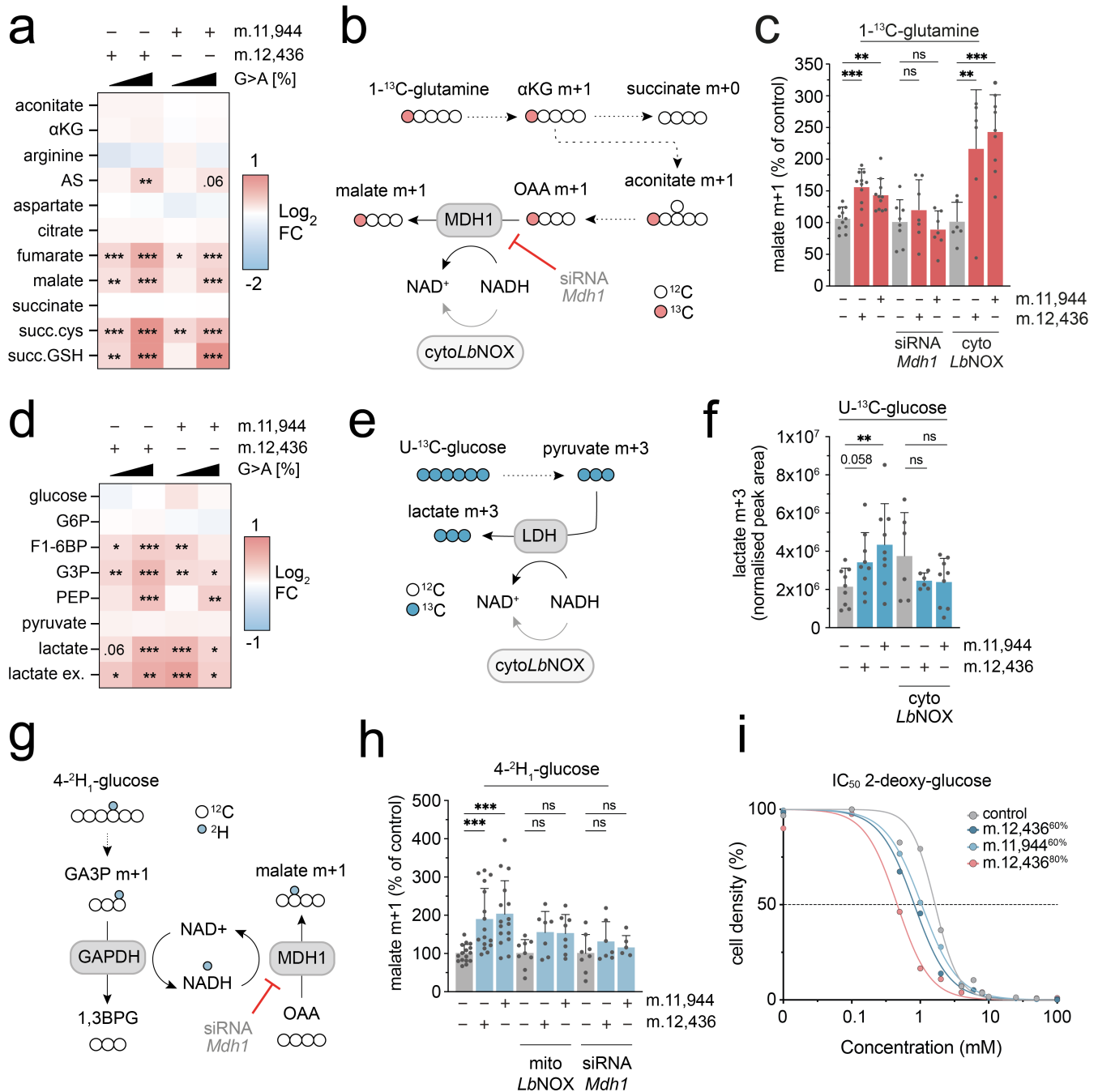
Mahmood et al - Figure 3
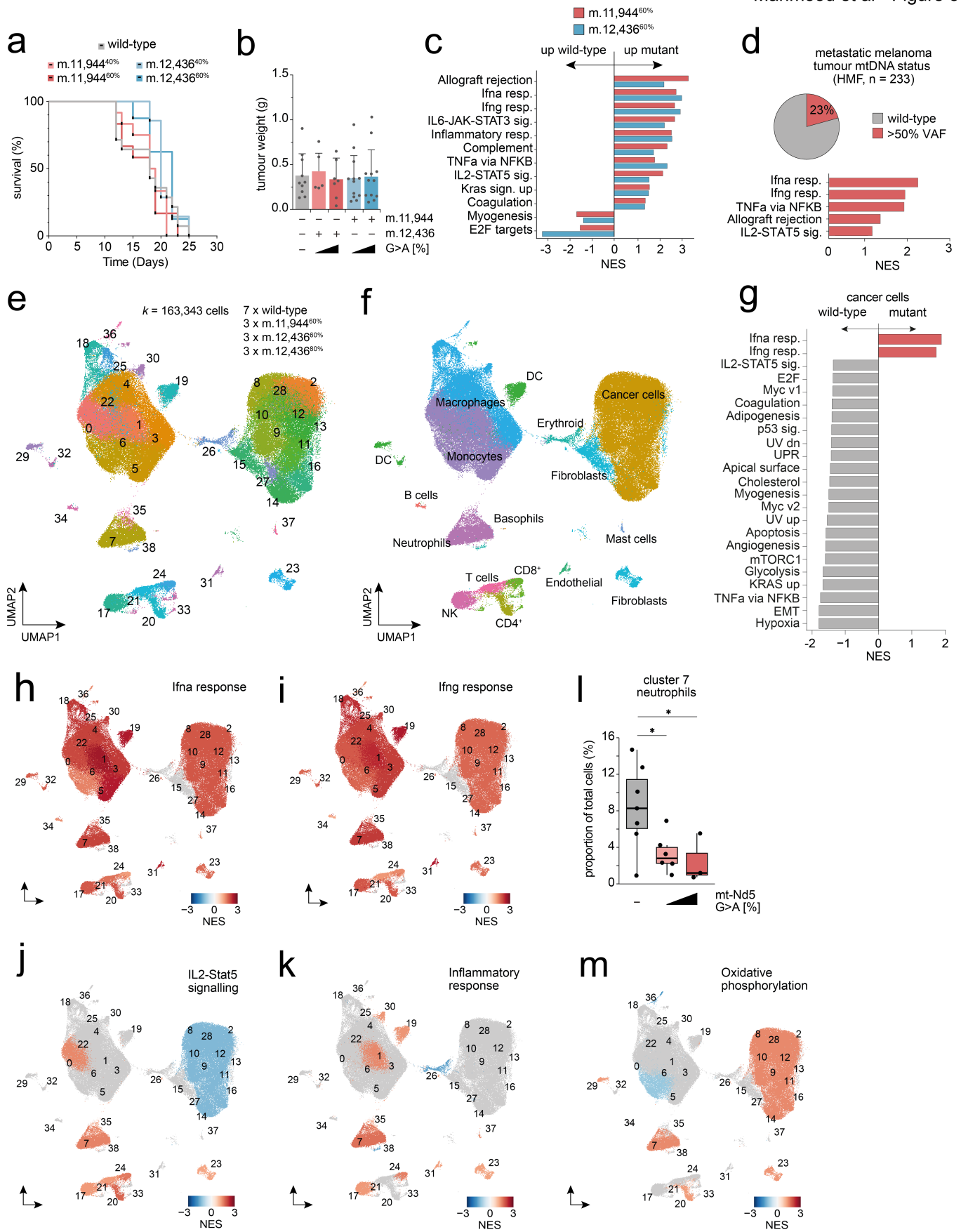
Mahmood et al - Figure 4
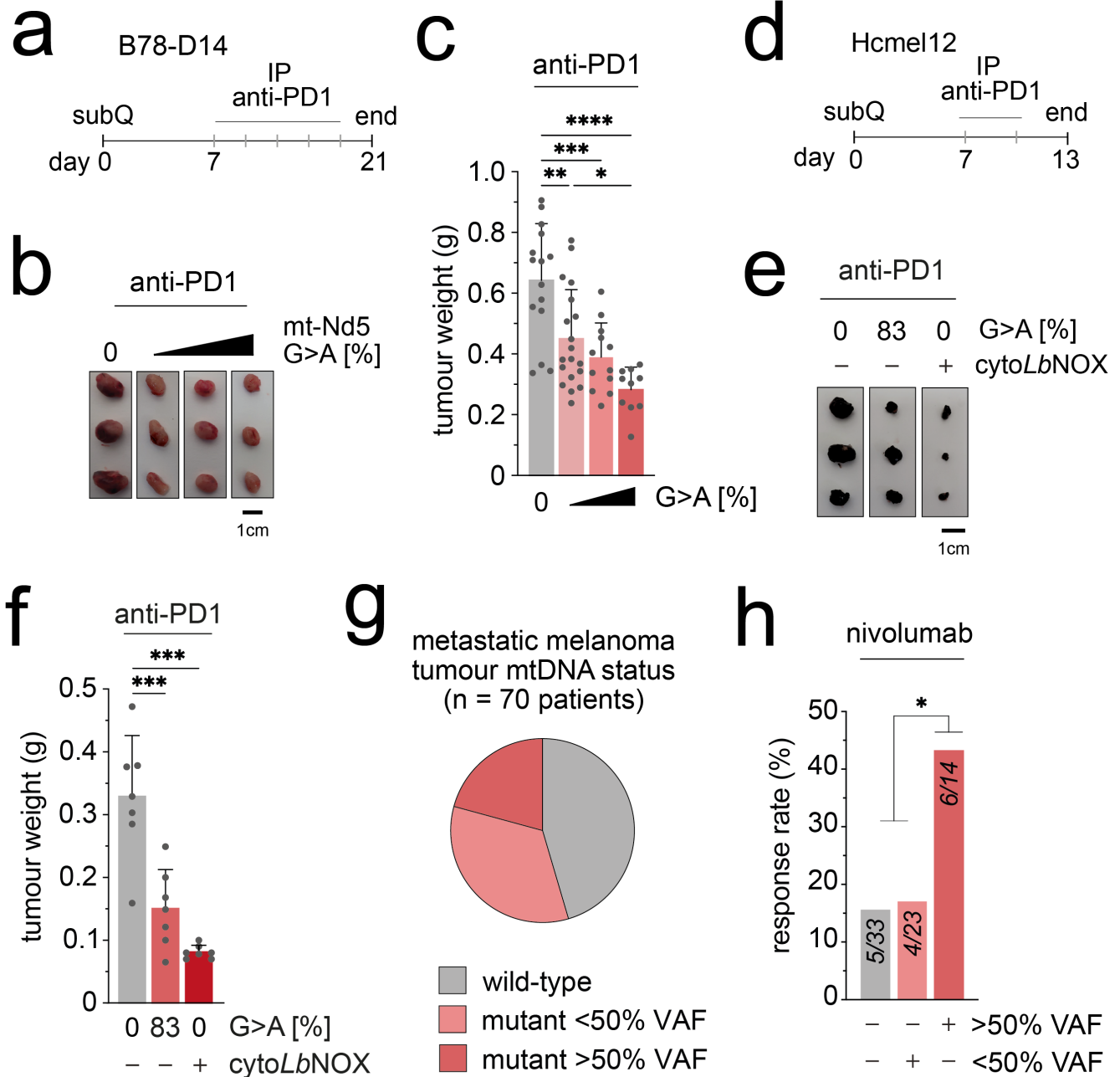
1   **Extended Data Figures**
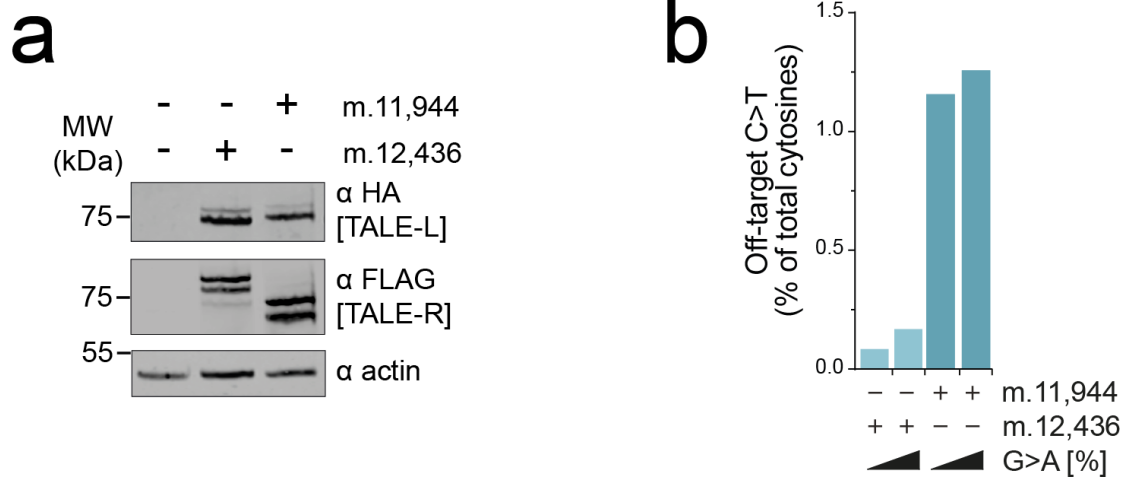
2

3   **Figure 1**. **Mitochondrial base editors for two independent targets in *mt-Nd5*. A**

4   Immunoblot of DdCBE pair expression post-sort. αHA and αFLAG show expression of

5   left (TALE-L) and right TALEs (TALE-R) respectively. Representative result is shown.

6   **B** Off-target C>T activity of DdCBEs on mtDNA by ultra-deep amplicon resequencing

7   of whole mtDNA. Figure depicts mutations detected at heteroplasmies >2% and is a

8   measure of mutations detected relative to wild-type. These mutations likely do not

9   impact our key observations as both models behave similarly across experiments.

10

11
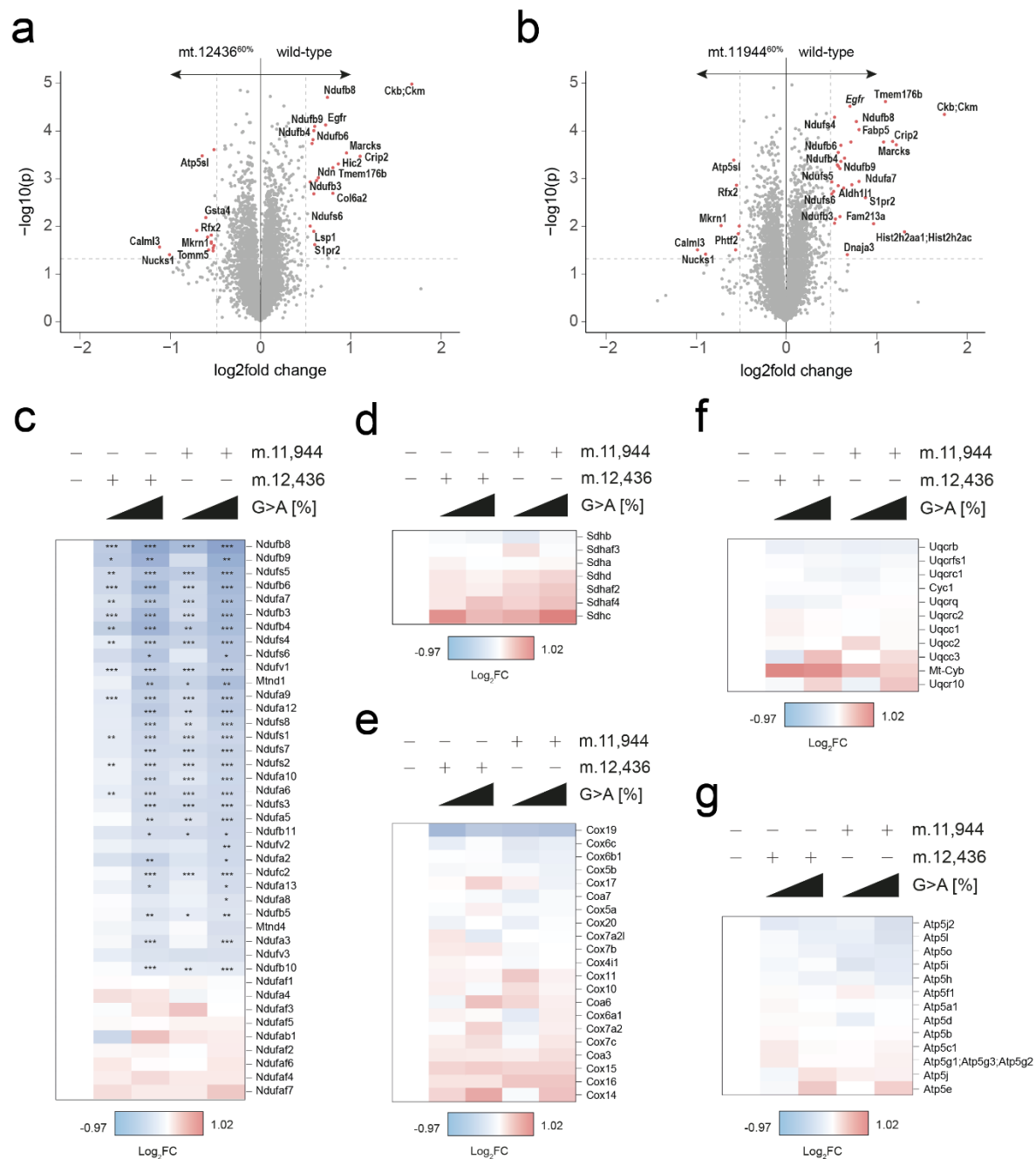
Figure 2. **Proteomic analysis of isogenic *mt-Nd5* mutant cell lines reveals significant changes primarily in complex I genes**. Volcano plot showing detected differences in protein abundance of **A** mt.12436$^{60\%}$ cells and **B** mt.11944$^{60\%}$ cells versus wild-type. Differences of $p < 0.05$ and $\log_2$ fold change > 0.5 shown in red (n=3 separately collected cell pellets were measured per cell line). Heatmaps of protein abundances for **C** complex I, **D** complex II, **E** complex III, **F** complex IV and **G** complex V nuclear and mitochondrial subunits. Wilcoxon signed rank test (A, B) and a one-way ANOVA test with Sidak multiple comparisons test (C-G) were applied
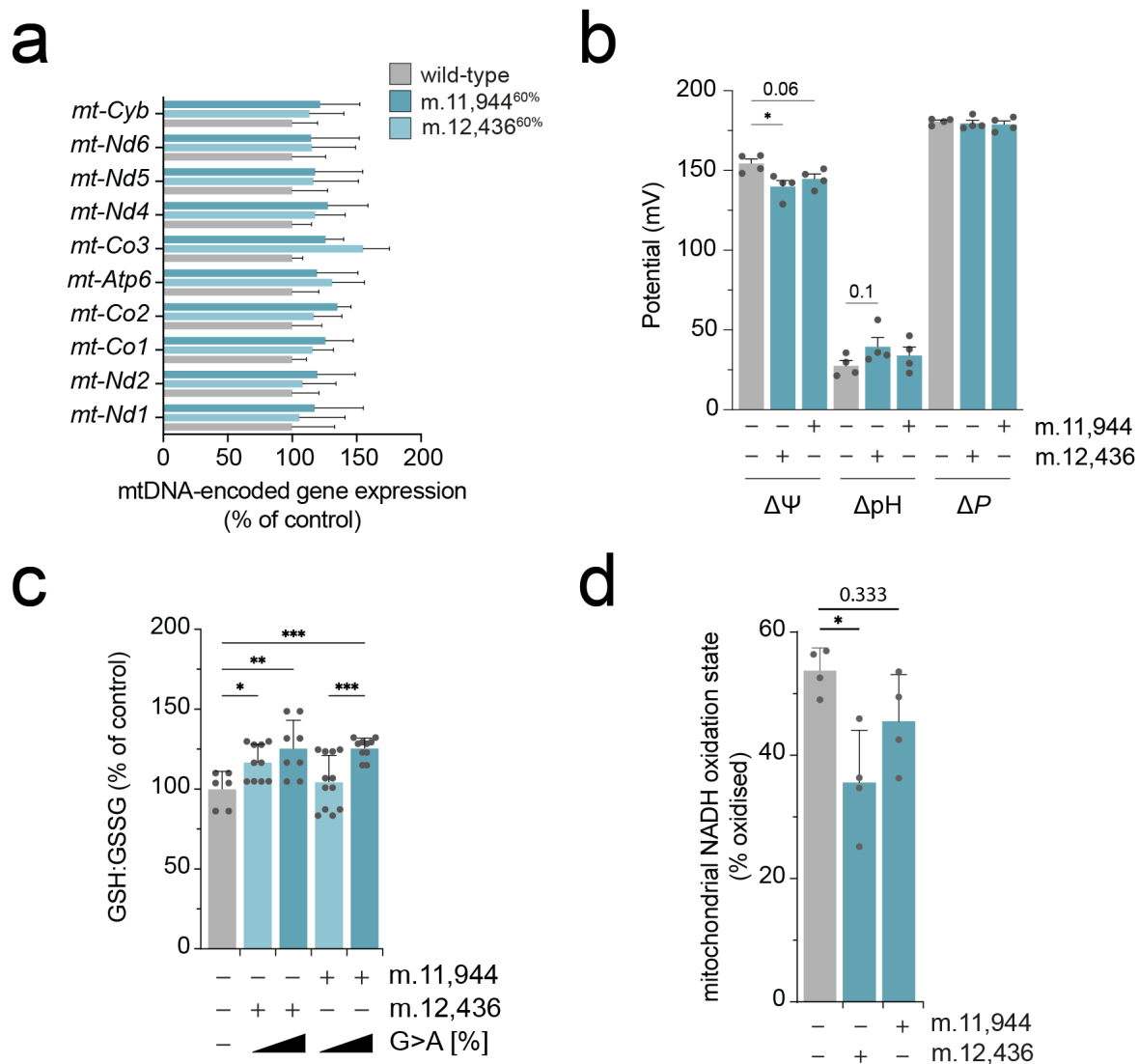
Figure 3. *mt.-Nd5* **truncations do not impact mitochondrial mRNA expression levels, but alter intracellular redox state and mitochondrial membrane potential**. **A** Expression of mitochondrial genes (n=12 separate cell pellets were sampled per genotype). **B** Measurements of the electrical component of the proton motive force, $\Delta\Psi$, the chemical component of the proton motive force ΔpH and total protonmotive force, ΔP (n=4 separate wells were sampled per genotype). **C** GSH : GSSG ratio (n= 6-12 separate wells were sampled per cell type). A high GSH : GSSG ratio represents a more reductive intracellular environment. **D** Mitochondrial NADH oxidation state (n=4 separate wells for sampled per genotype). All P-values were determined using a one-way ANOVA test with Sidak multiple comparisons test. Error bars indicate SD. Measure of centrality is mean.

33

34
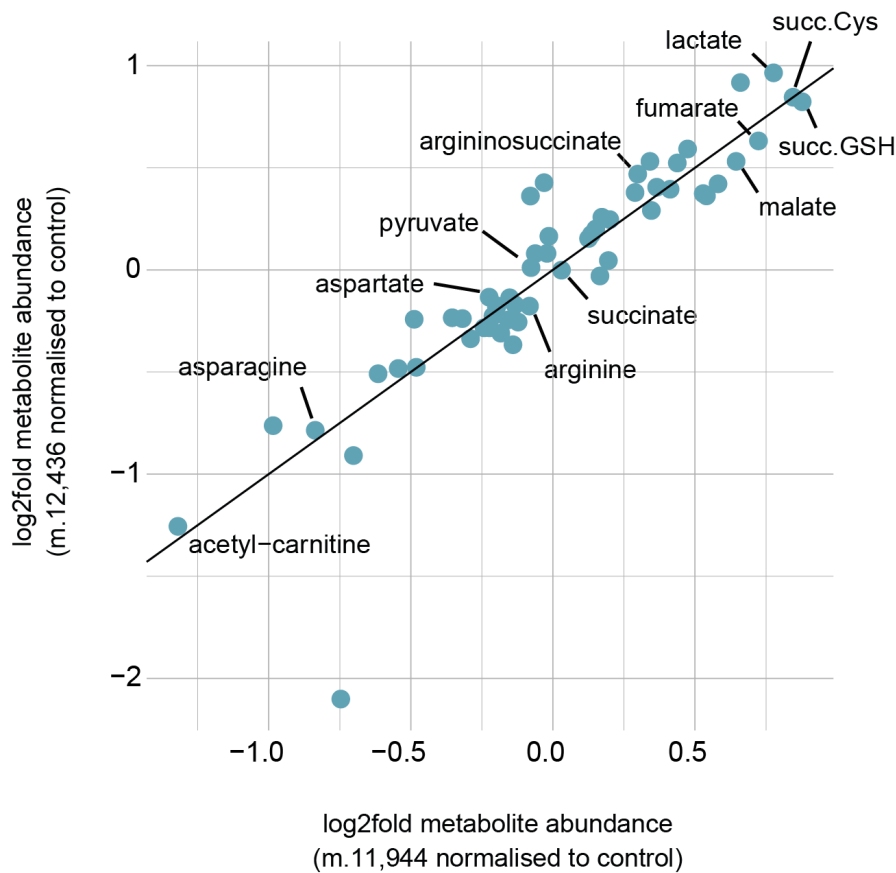
Figure 4. **Independent *mt-Nd5* truncations at matched heteroplasmy produce consonant changes in metabolite abundance**. Comparison of steady-state metabolite changes of m.12,436[60%] and m.11,944[60%] cells, each relative to wild-type (n= 6-9 separate wells per sample).

39
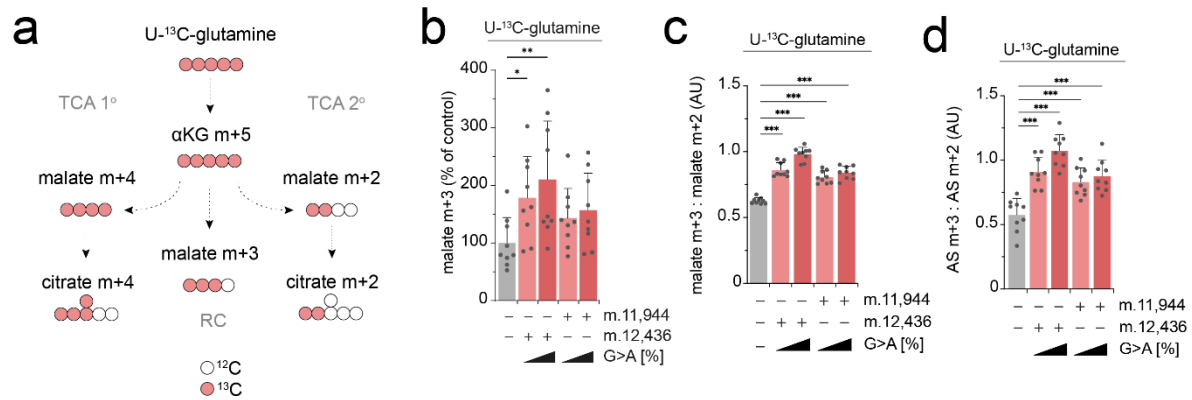
Figure 5. **U-^{13}C-glutamine labelling demonstrates that a proportion of the increased malate abundance is derived from cytosolic oxaloacetate**. **A** Labeling fate of ^{13}C derived from U-^{13}C-glutamine via oxidative decarboxylation versus reductive carboxylation of glutamine. **B** Malate m+3 abundance, derived from U-^{13}C-glutamine (n=9 separate wells were sampled per genotype). **C** malate m+3 : malate m+2 ratio, derived from U-^{13}C-glutamine (n= 9 separate wells were sampled per genotype). **D** AS m+3: AS m+2 ratio, derived from U-^{13}C-glutamine (n= 9 separate wells were sampled per genotype). All P-values were determined using a one-way ANOVA test with Sidak multiple comparisons test. Error bars indicate SD. Measure of centrality is mean.
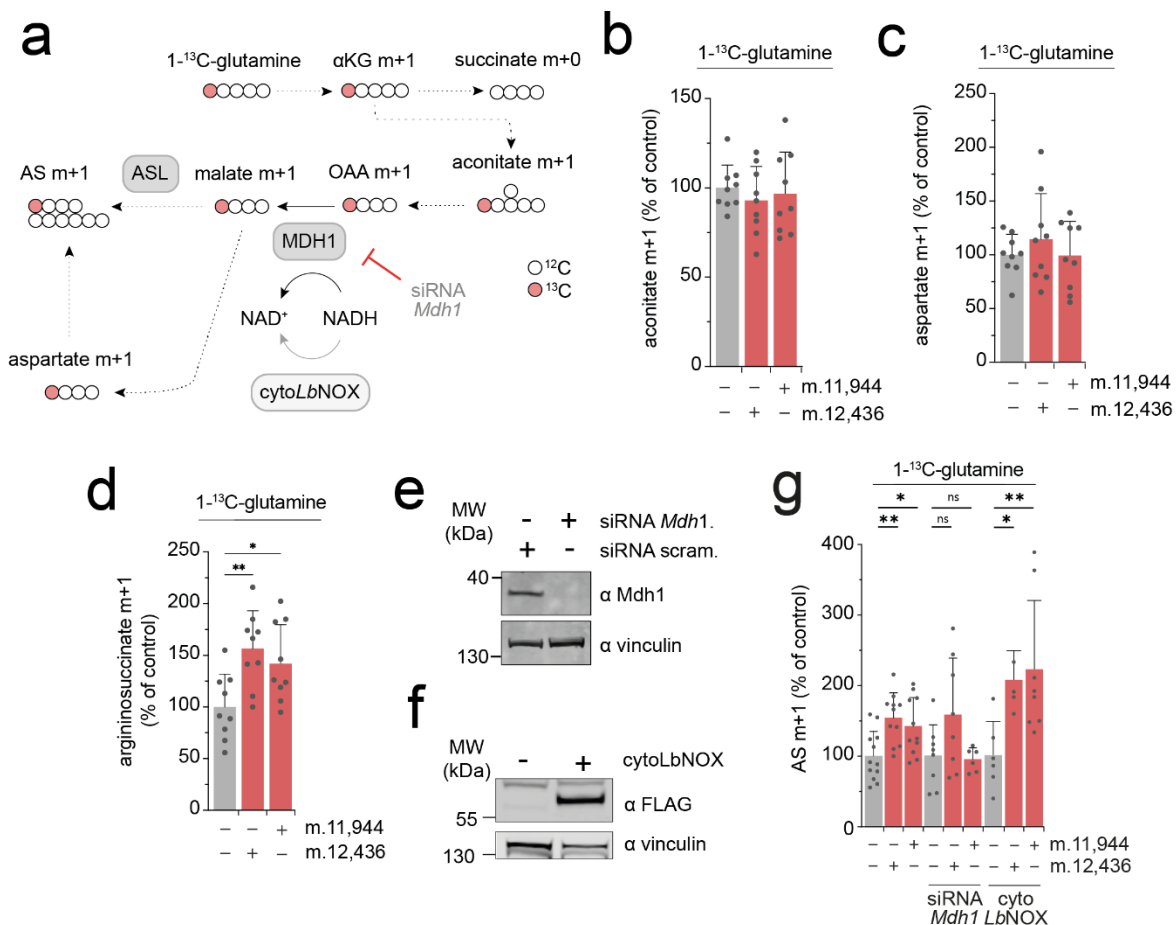
Figure 6. **Increased malate abundance occurs at the level of MDH1 but is not directly due to cytosolic redox potential**. **A** Labeling fate of ^{13}C derived from 1-^{13}C-glutamine which exclusively labels metabolites derived from the reductive carboxylation of glutamine. **B** Aconitate m+1 abundance, derived from 1-^{13}C-glutamine (n= 9 separate wells were sampled per genotype). **C** Aspartate m+1 abundance, derived from 1-^{13}C-glutamine (n= 9 separate wells were sampled per genotype). **D** AS m+1 abundance, derived from 1-^{13}C-glutamine (n= 9 separate wells were sampled per genotype). **E** Immunoblot of siRNA mediated depletion of *Mdh1*. Representative image shown. **F** Immunoblot of cytoLbNOX expression 36hrs post-sort, detected using αFLAG. Representative image shown. **G** AS m+1 abundance, derived from 1-^{13}C-glutamine with indicated treatment (n = 6-12 separate wells were sampled per genotype per condition). All P-values were determined using a one-way ANOVA test with Sidak multiple comparisons test. Error bars indicate SD. Measure of centrality is mean.
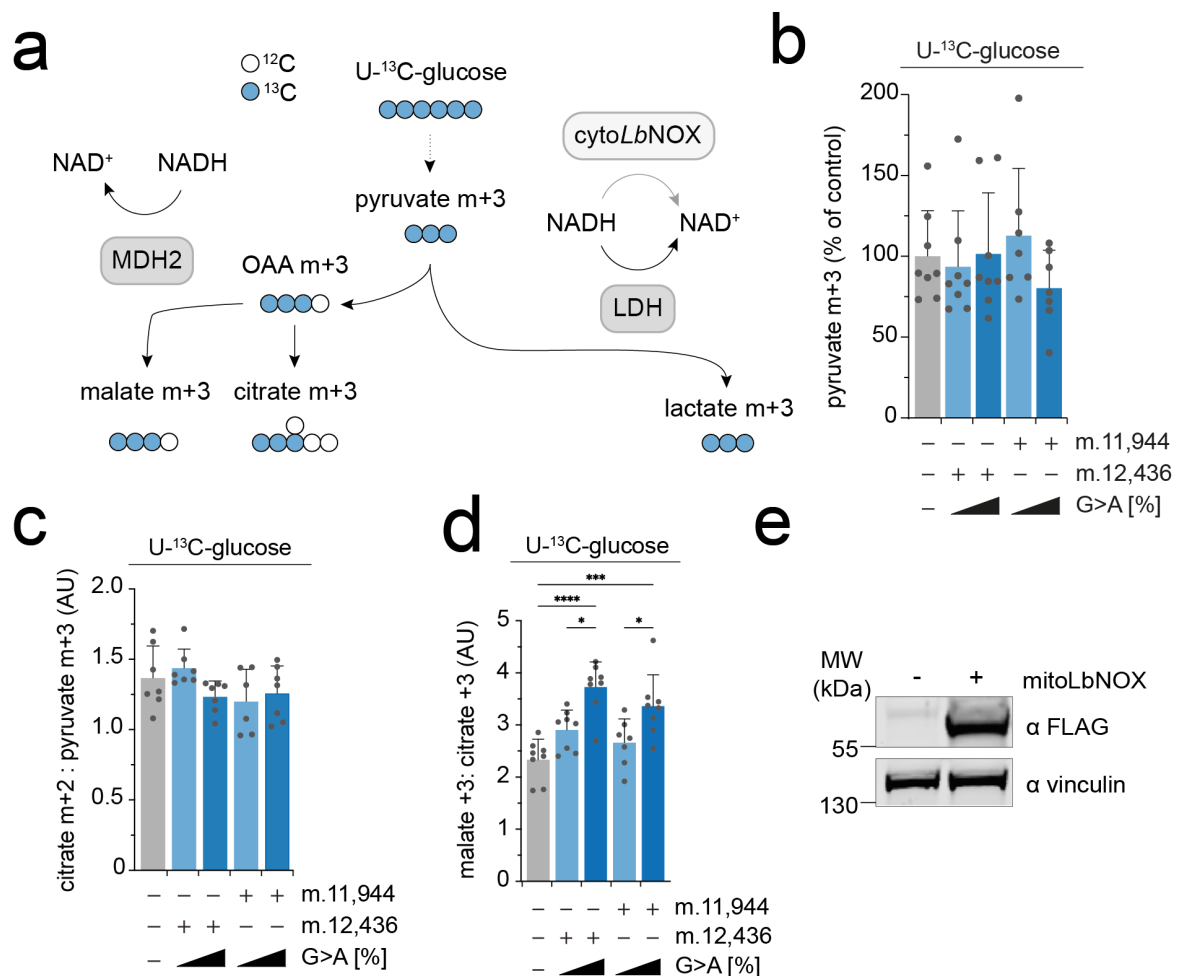
**Figure 7**. **Increased malate abundance in mutant cells is partially due to MDH2 reversal**. **A** Labeling fate of ^{13}C derived from U-^{13}C-glucose. **B** Pyruvate m+3 abundance, derived from U-^{13}C-glucose (n = 7-8 separate wells were sampled per genotype). **C** Citrate m+2 : pyruvate m+3 ratio, derived from U-^{13}C-glucose (n = 6-7 separate wells were sampled per genotype). **D** Malate m+3 : citrate m+3 ratio, derived from U-^{13}C-glucose (n = 7-8 separate wells were sampled per genotype). **E** Immunoblot of mitoLbNOX expression 36hrs post-transfection, detected using αFLAG. Representative image shown. All P-values were determined using a one-way ANOVA test with Sidak multiple comparisons test. Error bars indicate SD. Measure of centrality is mean.

83

84
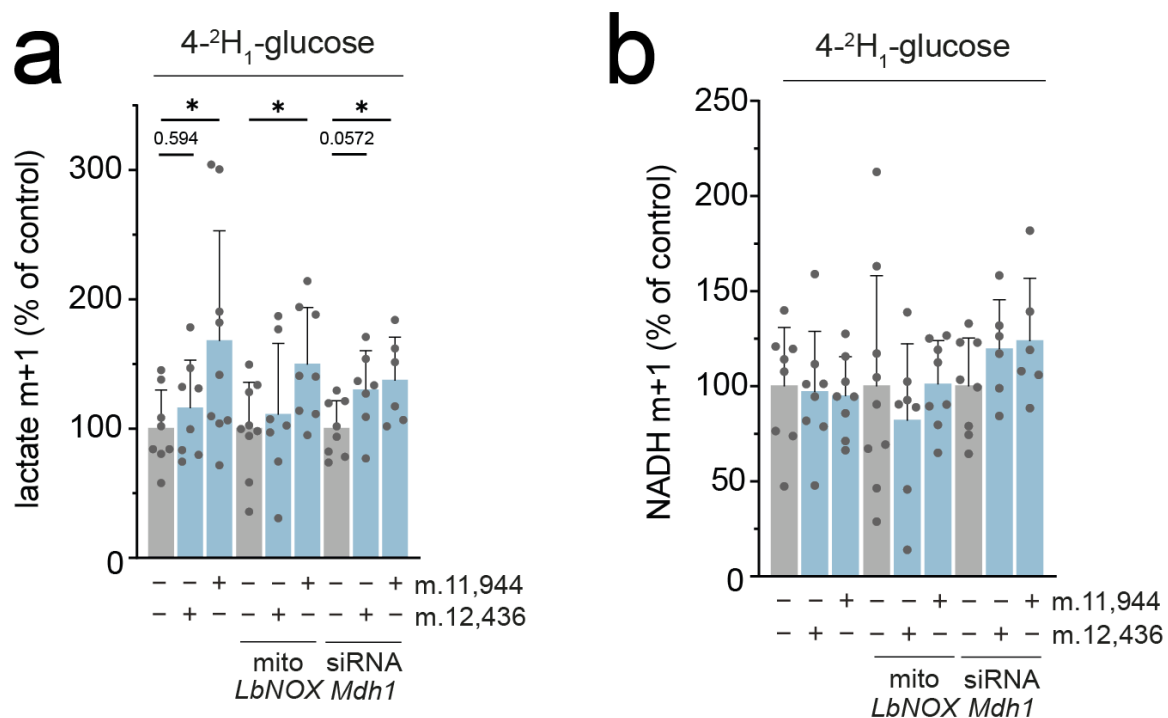
Figure 8. 4-^{2}H$_1$-glucose tracing demonstrates that shuttling of electrons between MDH1 and GAPDH drives aerobic glycolysis. **A** Lactate m+1 abundance, derived from 4-^{2}H$_1$-glucose with indicated treatment (n = 7-9 separate wells were sampled per genotype per condition). **B** NADH m+1 abundance, derived from 4-^{2}H$_1$-glucose with indicated treatment (n = 6-8 separate wells were sampled per genotype per condition). All P-values were determined using a one-way ANOVA test with Sidak multiple comparisons test. Error bars indicate SD. Measure of centrality is mean.

92
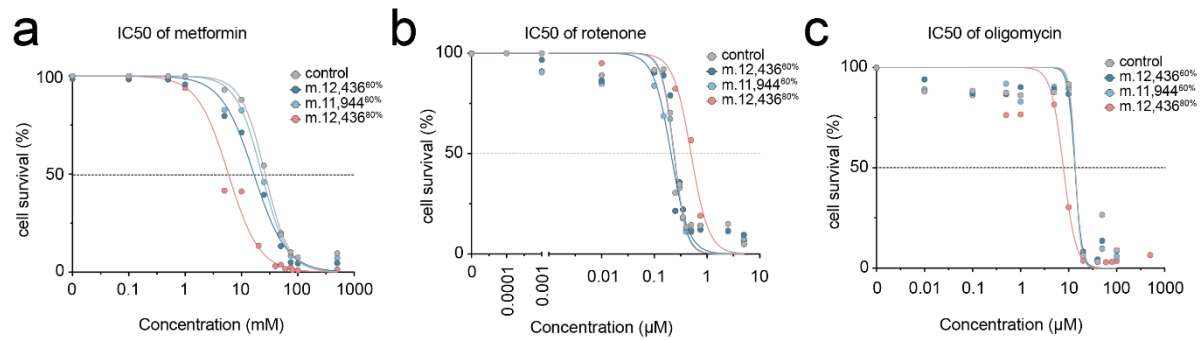
Figure 9. Mutant cells demonstrate a heteroplasmy dose-dependent sensitivity to respiratory chain inhibitors. A IC_{50} curve for metformin. IC_{50} for wild-type = 26.31 ± 1.49mM, for mt.12436[60%] = 16.60 ± 2.43mM, for mt.12436[80%] = 5.89 ± 0.71mM and for mt.11944[80%] = 22.93 ± 0.70mM **B** IC_{50} curve for rotenone. IC_{50} for wild-type = 0.236 ± 0.026µM, for mt.12436[60%] = 0.235 ± 0.035µM, for mt.12436[80%] = 0.493 ± 0.108µM and for mt.11944[60%] = 0.205 ± 0.033µM and **C** IC_{50} curve for oligomycin. IC_{50} for wild-type = 13.81 ± 3.80µM, for mt.12436[60%] = 13.52 ± 3.32µM, for mt.12436[80%] = 7.75 ± 0.56µM and for mt.11944[80%] = 13.54 ± 3.32µM (n = 4 separate wells per drug concentration per genotype). This was repeated 3 times and a representative result is shown.

111
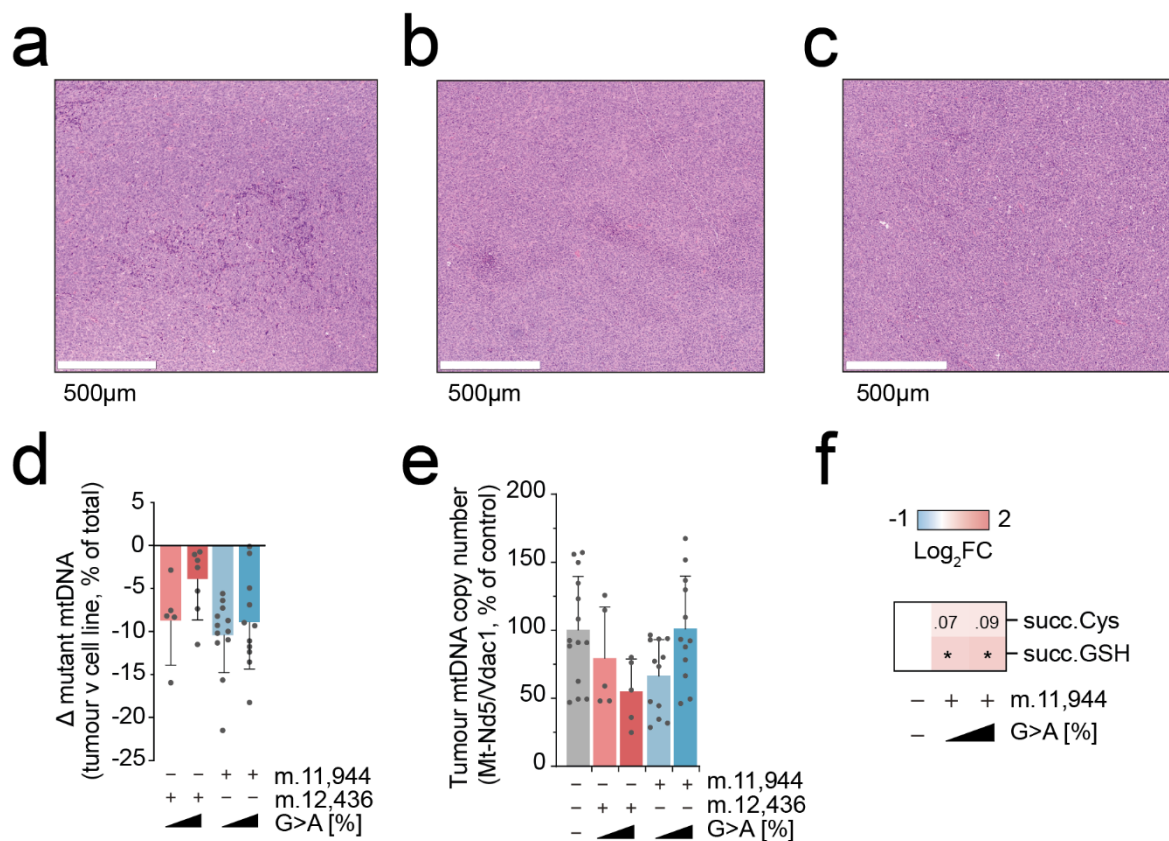
Figure 10: **Allografted B78-D14 lineage tumours do not exhibit macroscopic differences beyond metabolic indicators of disrupted MAS**. Representative H&E sub-section of **A** wild-type, **B** m.12,436[40%] and **C** m.12,436[60%] tumours. **D** Change in detected heteroplasmy in bulk tumour samples (n= 5-12 tumours per genotype). **E** Bulk tumour mtDNA copy number (n= 4-13 tumours per genotype). **F** Heatmap of steady-state abundance of metabolically terminal fumarate adducts, succinylcysteine and succinicGSH, demonstrating that metabolic changes observed *in vitro* are preserved *in vivo* (n= 12 tumours per genotype). All P-values were determined using a one-way ANOVA test with Sidak multiple comparisons test. Error bars indicate SD. Measure of centrality is mean.
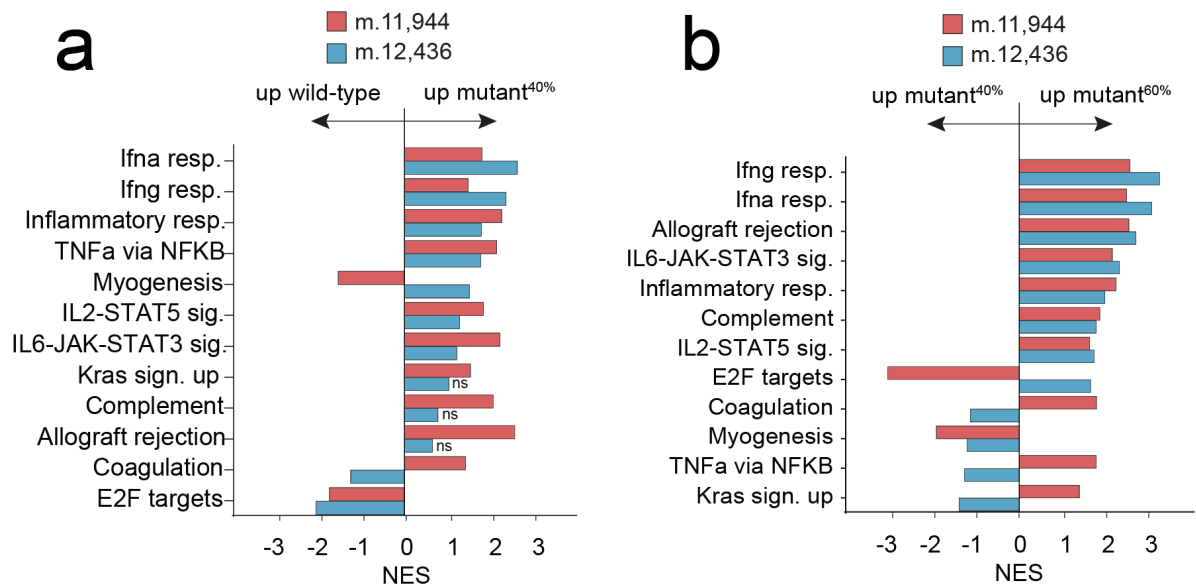
**Figure 11**. Bulk tumour transcriptional signatures show dose-dependent, heteroplasmy changes in immune-relevant transcriptional phenotypes. GSEA of bulk tumour RNAseq data (n=5-6 tumours per genotype) showing **A** mutant[40%] versus wild-type and **B** mutant[60%] versus mutant[40%]. Only genesets with adj. p-value <0.1 are shown unless otherwise stated. Wilcoxon signed rank test applied.
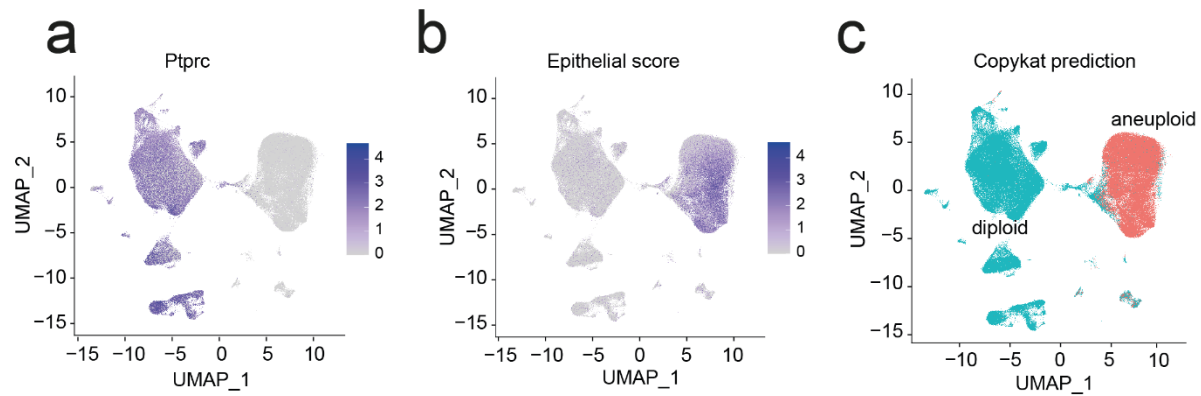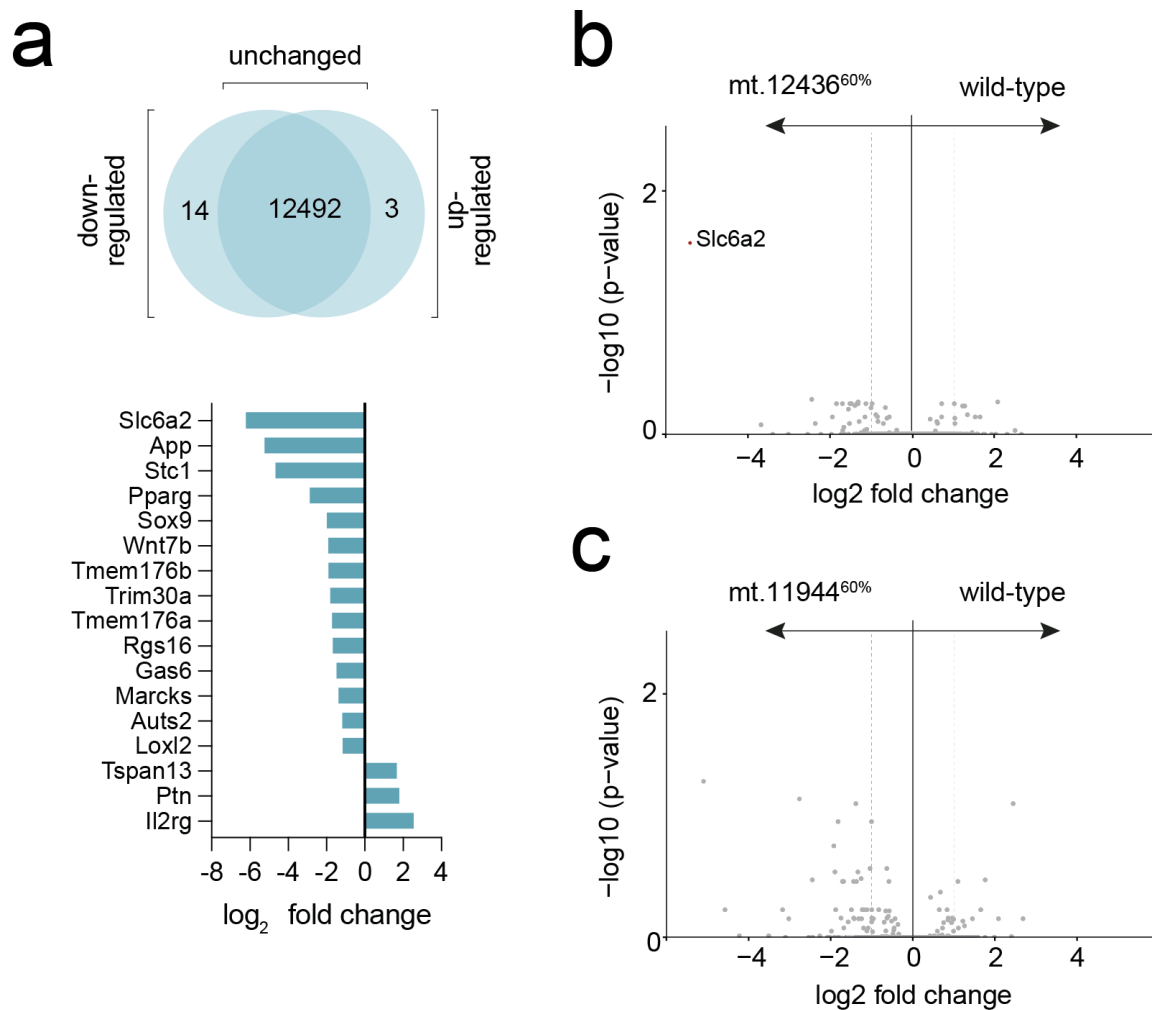
Figure 12. Malignant cells were defined in scRNAseq analysis as aneuploid cells with low or nil Ptprc (CD45) expression and high epithelial score. UMAP indicating **A** Ptprc expression, **B** epithelial score and **C** aneuploidy as determined by copykat prediction. These criteria were employed as the B78 cells lack distinct transcriptional signatures.

Figure 13. Mutant cells did not have significant changes in transcriptional signatures *in vitro*. **A** Significantly co-regulated transcripts from combined 60% mutant cells versus wild-type (n=12 cell pellets were sampled per genotype). Volcano plot showing differences in gene expression of **A** mt.12436$^{60\%}$ cells and **B** mt.11944$^{60\%}$ cells versus wild-type. Differences of $p < 0.05$ and $\log_2$ fold change > 1 shown in red (n=12 separate wells were sampled). Wilcoxon signed rank test applied.
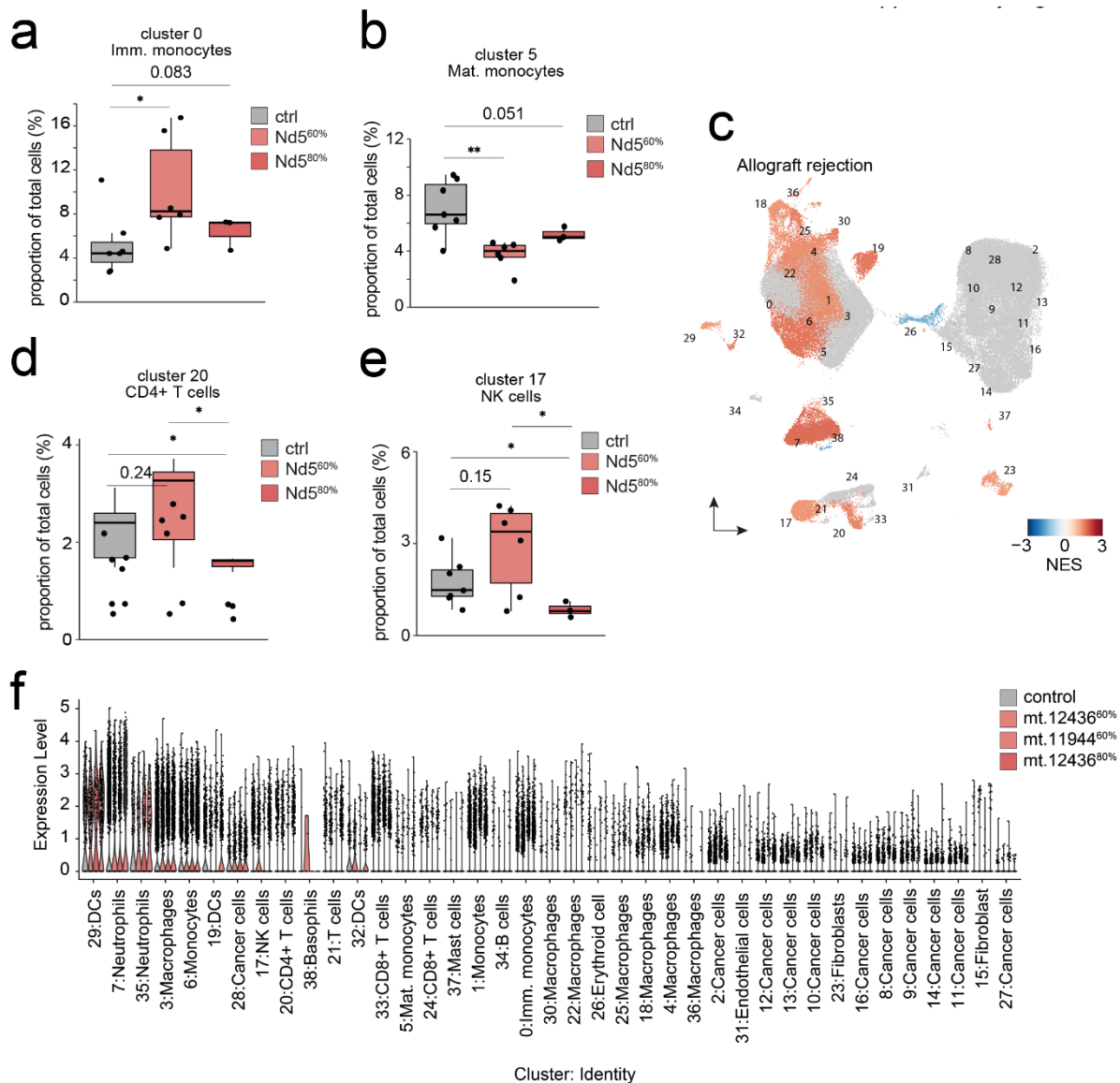
Figure 14. scRNAseq analyses reveal distinct alterations in the tumour immune microenvironment of mtDNA mutant tumours. Proportion of tumour resident: **A** immature monocytes; and **B** CD4+ T-cells relative to the total malignant and non-malignant cells (n = 3-7 tumours per genotype). **C** UMAP coloured by GSEA NES score for allograft rejection geneset. Proportion of tumour resident: **D** CD4+ T cells; and **E** natural killer (NK) cells relative to the total malignant and non-malignant cells (n = 3-7 tumours per genotype). **F** Relative PD-L1 expression within each cell (n = 3-7 tumours per genotype). One-way ANOVA test with Wilcoxon signed rank test (A) and two-tailed student's t-test (A-B, D-E) were applied. Error bars indicate SEM. Measure of centrality is mean. Box plots indicate interquartile range (A-B, D-E). NES: normalised expression score. DC, dendritic cell.
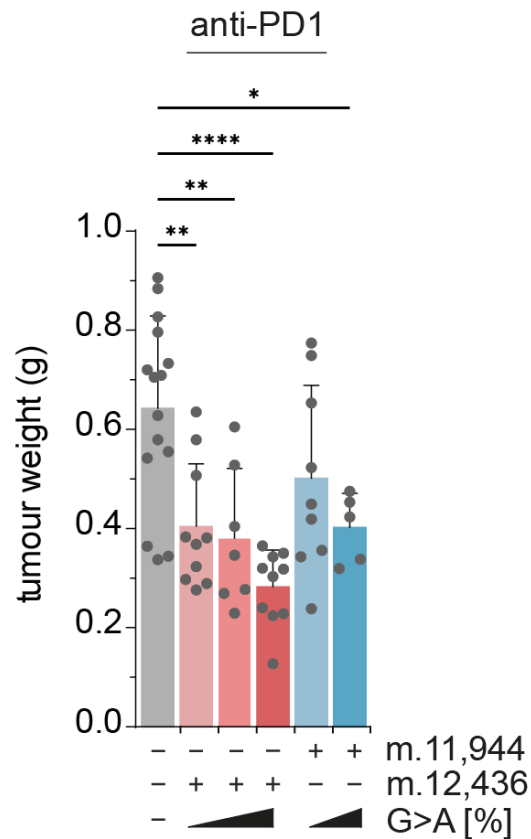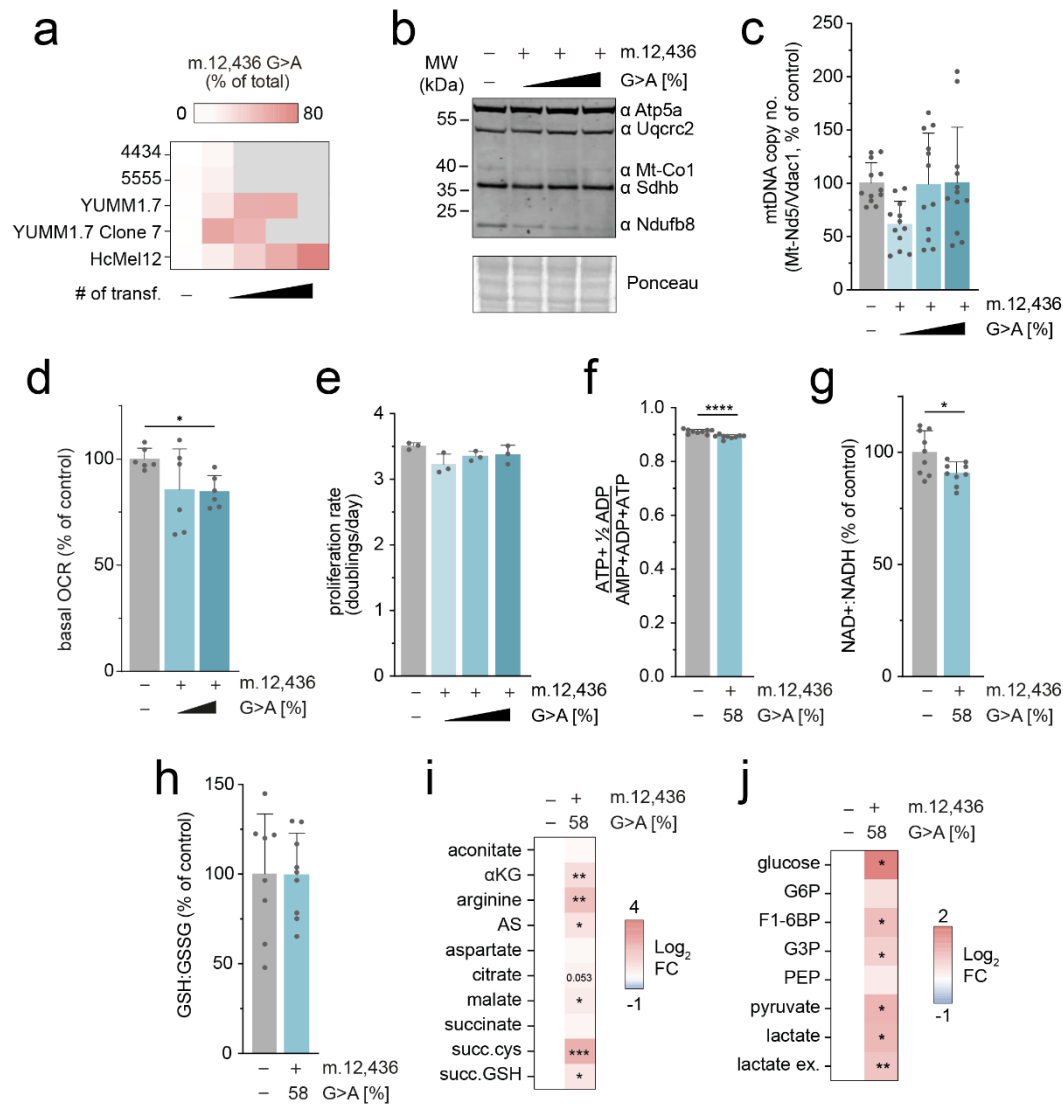
Figure 15. Remodelling of the tumour microenvironment in mutant cells sensitizes tumours to checkpoint blockade. Harvested tumour weight at day 21 (n= 5-15 tumours per genotype). One-way ANOVA test with Sidak multiple comparisons test was applied. Error bars indicate SD. Measure of centrality is mean.

Figure 16. HcMel12 mutant cells recapitulate the cellular and metabolic phenotypes observed in B78-D14 cells. A Heteroplasmy changes upon subsequent transfection of melanoma cell lines (n= 3 separate cell pellets per genotype). **B** Immunoblot of indicative respiratory chain subunits. Representative result is shown. **C** mtDNA copy number (n= 12 separate wells per genotype). **D** Basal oxygen consumption rate (OCR) (n = 6 measurements (12 wells per measurement) per genotype). **E** Proliferation rate of cell lines in permissive growth media (n = 3 separate wells per genotype) **F** Energy (adenylate) charge state (n = 9 separate wells per genotype). **G** NAD+:NADH ratio (n= 9 separate wells per genotype). **H** GSH : GSSG ratio (n= 8-9 separate wells per genotype). **I** Heatmap of unlabelled steady-state abundance of select mitochondrial metabolites, arginine, argininosuccinate (AS) and terminal fumarate adducts succinylcysteine (succ. Cys) and succinicGSH (succ.GSH)

177   (n= 9 separate wells per genotype). **J** Heatmap of unlabelled steady-state metabolite

178   abundances for select intracellular glycolytic intermediates and extracellular lactate

179   (ex. lactate) (n= 9 separate wells per genotype). P-values were determined using a

180   one-way ANOVA test with (C-D) Sidak multiple comparisons test, Fisher's LSD Test

181   (E)or (F-J) a one-tailed student's t-test. Error bars indicate SD. Measure of centrality

182   is mean.

183
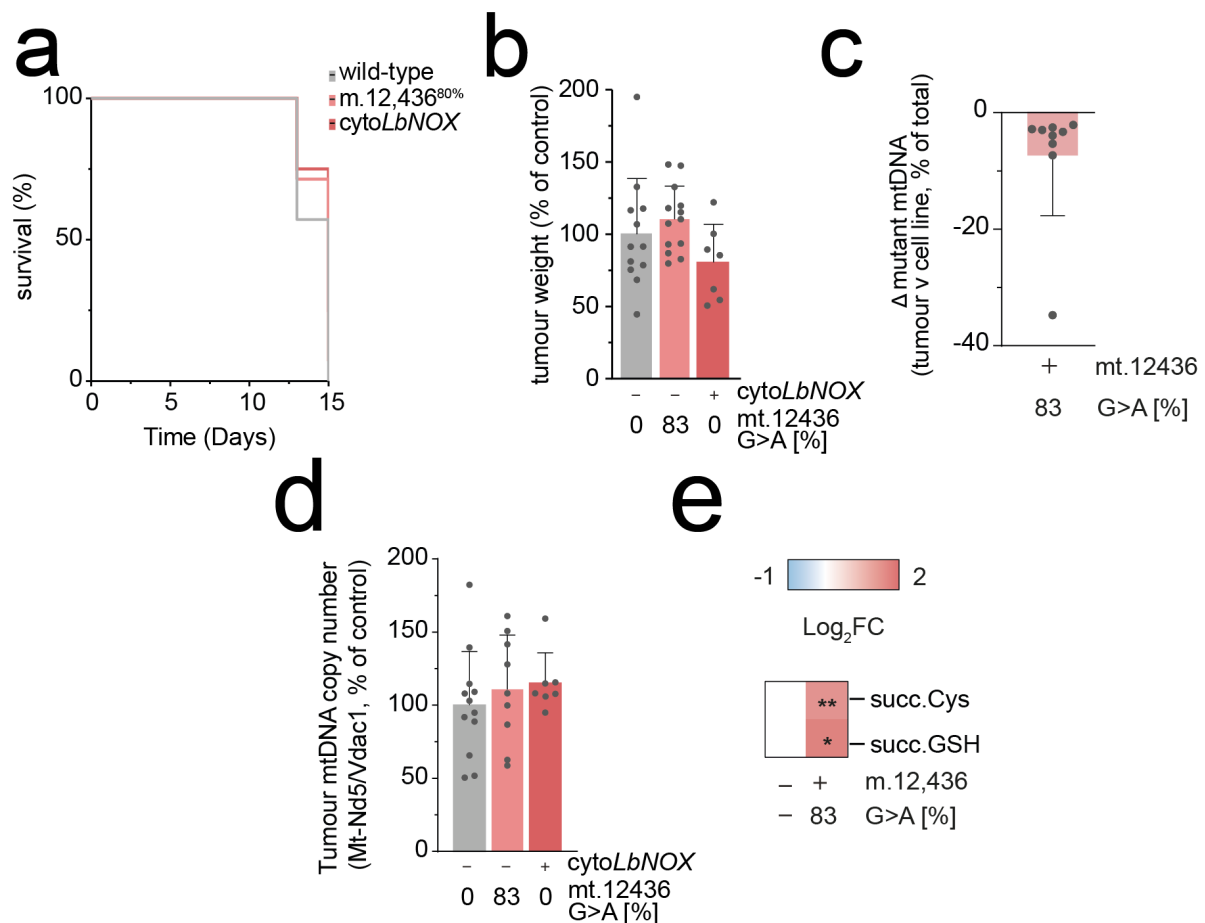
Figure 17. Untreated Hcmel12 lineage tumours recapitulate B78-D14 lineage. A Survival of C57/BL6 mice subcutaneously injected with indicated cells (n = 9-10 animals per genotype). **B** Tumour weight at endpoint (n = 9-10 tumours per genotype). **C** Change in detected heteroplasmy in bulk tumour samples (n= 9 tumours per genotype). **D** Bulk tumour mtDNA copy number (n= 9 tumours per genotype). **E** Heatmap of steady-state abundance of metabolic terminal fumarate adducts, succinylcyst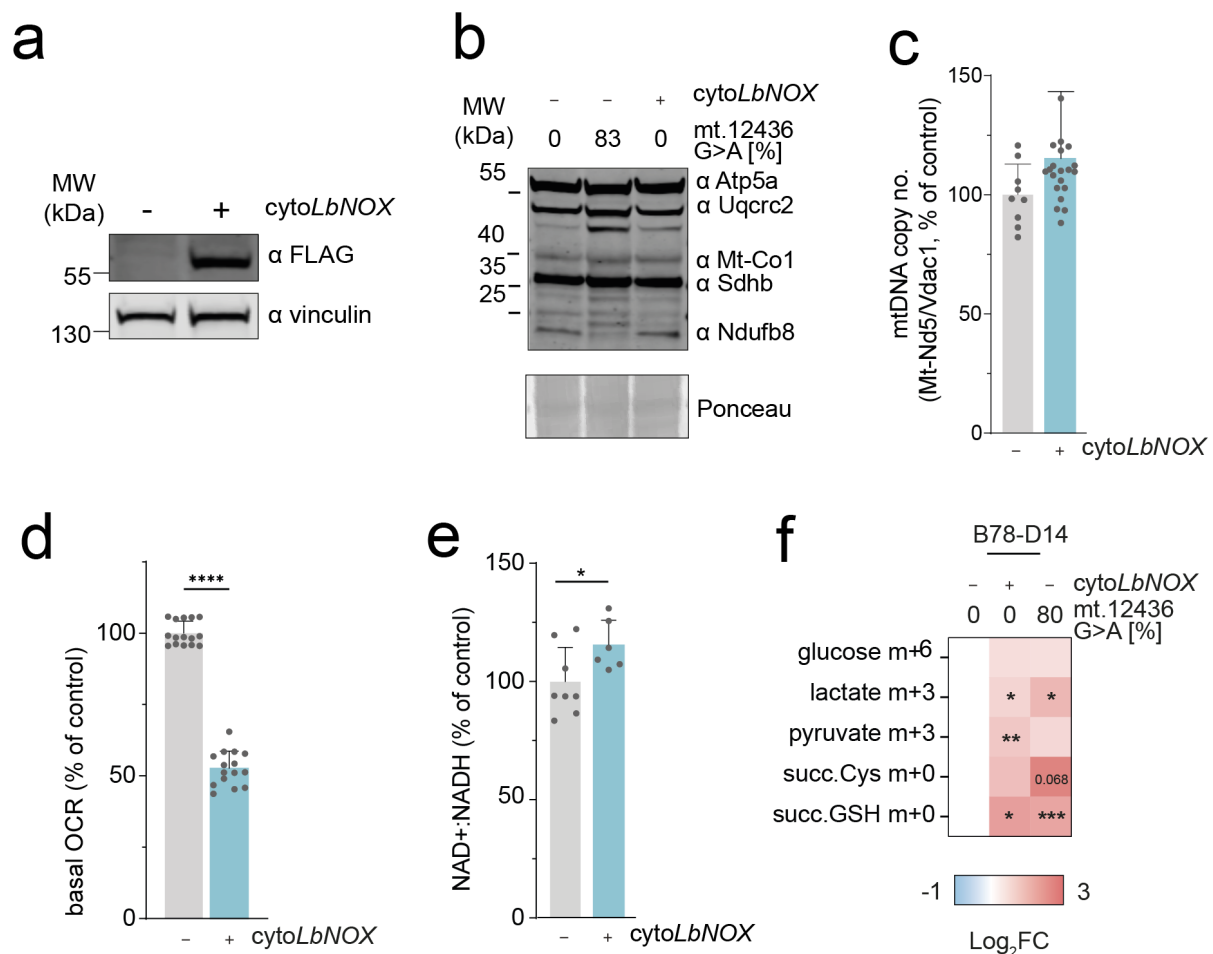eine and succinicGSH, demonstrating that metabolic changes observed in B78 mutant tumours are preserved *in vivo* (n= 9 tumours per genotype). P-values were determined using a one-way ANOVA test with (B,D) Sidak multiple comparisons test or student's one-tailed t-test (E). Error bars indicate SD. Measure of centrality is mean.

Figure 18. Constitutive expression of cyto*Lb*NOX phenocopies metabolic changes observed in *mt-Nd5* mutant cells. A. Immunoblot of cyto*Lb*NOX expression in clonal population, detected using αFLAG. Representative image shown. **B**. Immunoblot of indicative respiratory chain subunits. Representative result is shown. **C.** mtDNA copy number (n= 9 separate wells per genotype). **D** Basal oxygen consumption rate (OCR) (n = 9-15 measurements (6 wells per measurement) per genotype) A significant decrease is observed in HcMel12 cyto*Lb*NOX, akin to the decrease in basal OCR measured in m.12,436[80%] cells. **E.** NAD+:NADH ratio (n= 11-12 separate wells per genotype). **F.** Heatmap of metabolite abundance of glucose m+3, lactate m+3, pyruvate m+3, and terminal fumarate adducts succinylcysteine (succ. Cys) and succinicGSH (succ.GSH) in U-^{13}C-glucose labelling of B78 cells. B78 wild-type cells were transiently transfected with cyto*Lb*NOX and metabolites were extracted 3 days post-sort. A significant increase in lactate abundance was observed in cyto*Lb*NOX-expressing cells mimicking that observed in m.12,436[80%] cells. (n= 9-13 separate wells per

213   genotype). All P-values were determined using a one-paired student's t-test. Error

214   bars indicate SD. Measure of centrality is mean.

215

216   **Extended Data Methods**

217   mtDNA sequencing

218   Cellular DNA was amplified to create two ~8kbp overlapping mtDNA products using

219   PrimeStar GXL DNA Polymerase (Takara Bio) as per the manufacturer's instructions.

220

221   Primers

222   Forward 1: 5'-ACTGATATTACTATCCCTAGGAGG-3'

223   Reverse 1: 5'-TTTGAGTAGAACCCTGTTAGG-3'

224   Forward 2: 5'-GGCCTGATAATAGTGACGC-3'

225   Reverse 2: 5'-GGTTGGGTTTAGTTTTTGTTTGG-3'

226

227   Resulting amplicons were sequenced using Illumina Nextera kit (150 cycle, paired-

228   end). To determine the percentage of non-target C mutations in mtDNA, we first

229   identified all C/G nucleotides with adequate sequencing coverage (>1000X) in both

230   the reference and experimental sample. Then, for each of the 4 experimental samples,

231   we identified positions for which sequencing reads in the experimental sample

232   corresponded to G>A/C>T mutations. We further filtered the resulting list of mutations

233   to retain only those with a heteroplasmy over 2%, and removed mutations that were

234   also present in control samples. Finally, the non-target percentage was calculated as

235   the fraction of total possible C/G positions that were mutated.

236

237   Sample preparation for MS analysis

238   Cells were lysed in a buffer containing 4% SDS in 100 mM Tris-HCl pH 7.5 and 55

239   mM iodoacetamide. Samples were then prepared as previously described in [23] with

240   minor modifications. Alkylated proteins were digested first with Endoproteinase Lys-C

241   (1:33 enzyme:lysate) for 1hr, followed by an overnight digestion with trypsin (1:33

242   enzyme:lysate). Digested peptides from each experimental condition and a pool

243   sample were differentially labelled using TMT16-plex reagent (Thermo Scientific) as

244   per the manufacturer's instructions. Fully labelled samples were mixed in equal

245   amount and desalted using 100 mg Sep Pak C18 reverse phase solid-phase extraction

246   cartridges (Waters). TMT-labelled peptides were fractionated using high pH reverse

247   phase chromatography on a C18 column (150 × 2.1 mm i.d. - Kinetex EVO (5 μm, 100

248   Å)) on a HPLC system (LC 1260 Infinity II, Agilent). A two-step gradient was applied,

249   1% to 28% B (80% acetonitrile) over 42 min, then from 28% to 46% B over 13 min to

250   obtain a total of 21 fractions for MS analysis

251

252   <u>UHPLC-MS/MS analysis</u>

253   Peptides were separated by nanoscale C18 reverse-phase liquid chromatography

254   using an EASY-nLC II 1200 (Thermo Scientific) coupled to an Orbitrap Fusion Lumos

255   mass spectrometer (Thermo Scientific). Elution was carried out using a binary gradient

256   with buffer A (water) and B (80% acetonitrile), both containing 0.1% formic acid.

257   Samples were loaded with 6 μl of buffer A into a 50 cm fused silica emitter (New

258   Objective) packed in-house with ReproSil-Pur C18-AQ, 1.9 μm resin (Dr Maisch

259   GmbH). Packed emitter was kept at 50 °C by means of a column oven (Sonation)

260   integrated into the nanoelectrospray ion source (Thermo Scientific). Peptides were

261   eluted at a flow rate of 300 nl/min using different gradients optimised for three sets of

262   fractions: 1–7, 8–15, and 16–21[23]. Each fraction was acquired for a duration of

263   185 minutes. Eluting peptides were electrosprayed into the mass spectrometer using

264   a nanoelectrospray ion source (Thermo Scientific). An Active Background Ion

265   Reduction Device (ESI Source Solutions) was used to decrease air contaminants

266   signal level. The Xcalibur software (Thermo Scientific) was used for data acquisition.

267   A full scan over mass range of 350–1400 m/z was acquired at 60,000 resolution at

268   200 m/z, with a target value of 500,000 ions for a maximum injection time of 50 ms.

269   Higher energy collisional dissociation fragmentation was performed on most intense

270   ions during 3 sec cycle time, for a maximum injection time of 120 ms, or a target value

271   of 100,000 ions. Peptide fragments were analysed in the Orbitrap at 50,000 resolution.

272

273   <u>Proteomics Data Analysis</u>

274   The MS Raw data were processed with MaxQuant software[24] v.1.6.1.4 and searched

275   with Andromeda search engine[25], querying SwissProt[26] *Mus musculus* (25,198

276   entries). First and main searches were performed with precursor mass tolerances of

277   20 ppm and 4.5 ppm, respectively, and MS/MS tolerance of 20 ppm. The minimum

278   peptide length was set to six amino acids and specificity for trypsin cleavage was

279   required, allowing up to two missed cleavage sites. MaxQuant was set to quantify on

280   "Reporter ion MS2", and TMT16plex was set as the Isobaric label. Interference

281 between TMT channels was corrected by MaxQuant using the correction factors

282 provided by the manufacturer. The "Filter by PIF" option was activated and a "Reporter

283 ion tolerance" of 0.003 Da was used. Modification by iodoacetamide on cysteine

284 residues (carbamidomethylation) was specified as variable, as well as methionine

285 oxidation and N-terminal acetylation modifications. The peptide, protein, and site false

286 discovery rate (FDR) was set to 1 %. The MaxQuant output ProteinGroup.txt file was

287 used for protein quantification analysis with Perseus software[27] version 1.6.13.0. The

288 datasets were filtered to remove potential contaminant and reverse peptides that

289 match the decoy database, and proteins only identified by site. Only proteins with at

290 least one unique peptide and quantified in all replicates in at least one experimental

291 group were used for analysis. Missing values were added separately for each column.

292 The TMT corrected intensities of proteins were normalised first by the median of all

293 intensities measured in each replicate, and then by using LIMMA plugin[28] in Perseus.

294 Significantly regulated proteins between two groups were selected using a

295 permutation-based Student's t-test with FDR set at 1%.

296

297 Mitochondrial membrane potential and pH gradient

298 Membrane potential and pH gradient were measured using multi-wavelength

299 spectroscopy as described in [29-30]. Briefly, cultured cells were disassociated by

300 gentle tapping and then spun down and resuspended at a density of 1×10^7 cells/mL

301 in FluroBrite supplemented with 2 mM glutamine in a temperature-controlled

302 chamber. Changes in mitochondrial cytochrome oxidation states were then

303 measured with multi-wavelength spectroscopy. The baseline oxidation state was

304 measured by back-calculation using anoxia to fully reduce the cytochromes, and a

305 combination of 4μM FCCP and 1μM rotenone to fully oxidize the cytochromes. The

306 membrane potential was then calculated from the redox poise of the b-hemes of the

307 bc_1 complex and the pH gradient measured from the turnover rate and redox span of

308 the bc_1 complex using a model of turnover[30].

309

310 Mitochondrial NADH oxidation state

311 Changes in NAD(P)H fluorescence were measured simultaneously with

312 mitochondrial membrane potential using 365nm excitation. The resultant emission

313 spectrum was then measured with multi-wavelength spectroscopy[29]. The baseline

314 oxidation state of the mitochondrial NADH pool was back calculated using anoxia to

315   fully reduce, and 4 µM FCCP to fully oxidize the mitochondrial NADH pool,

316   respectively, assuming the cytosolic NADH pool and NADPH pools did not change

317   with these interventions and short time period.

318

319   <u>H&E Staining</u>

320   Haematoxylin and Eosin (H&E) staining and slide scanning was performed as

321   described in [31].

322

323   <u>scRNAseq Methodology</u>

324   **1-**Preprocessing of single-cell RNA transcriptomics data, batch effect correction, and

325   clustering

326   CellRanger (v.7.0.1) was used to map the reads in the FASTQ files to the mouse

327   reference genome (GRCm39)[32]. Seurat (v.4.2.0) package in R (v.4.2.1) was used to

328   handle the pre-processed gene counts matrix generated by cellRanger[33]. As an initial

329   quality control step, cells with fewer than 200 genes as well as genes expressed in

330   less than 3 cells were filtered out. Cells with >5% mitochondrial counts, UMI counts >

331   37000, and gene counts < 500 were then filtered out. The filtered gene counts matrix

332   (31647 genes and 127356 cells) was normalized using the NormalizeData function

333   using the log(Normalization) method and scale.factor to 10000. The

334   FindVariableFeatures function was used to identify 2000 highly variable genes for

335   principal component analysis. The first 50 principal components were selected for

336   downstream analysis. RunHarmony function from harmony package (v.0.1.0) with

337   default parameters was used to correct batch effects[34]. The RunUMAP function with

338   the reduction from "harmony" was used to generate UMAPs for cluster analysis.

339   FindClusters function was used with the resolution parameters set to 1.6.

340

341   2-Epithelial score

342   Average gene expression from cytokeratins, Epcan, and Sfn were used to calculate

343   epithelial score.

344

345   **3-**Single-cell copy number estimation

346   CopyKat (v.1.1.0) was used to estimate the copy number status of each cell[14].

347   Parameters were set as ngene.chr=5, win.size=25, KS.cut=0.1, genome="mm10" and

348   cells annotated as T cells or NK cells in the UMAP as diploid reference cells.

349

350   4-Identification of differential expressed marker genes

351   Top differentially expressed genes in each cluster were identified using the

352   FindAllMarkers function in the Seurat R package. Parameters for expression

353   difference were set to be at least 1.25 times of fold changes (logfc.threshold = 1.25)

354   and adjusted p-value < 0.05 with gene expression detected in at least 10% of cells in

355   each cluster (min.pct = 0.1). The top 20 highly differentially expressed genes in each

356   cluster ranked by average fold change were defined as marker genes.

357

358   5-Pathway enrichment analysis of single-cell transcriptomics data

359   For cells in each identified cluster in the UMAP, the wilcoxauc function from presto R

360   package (version 1.0.0) was used to conduct wilcox rank-sum test to obtain the fold

361   change and p-value for all genes between cells in the high heteroplasmy group for

362   both mutations and control group[35]. The genes were ranked in decreasing order

363   according to the formula $\text{sign}(\log_2 FC) * (-\log_{10}(\text{p-value}))$. This ranked gene list, and

364   mouse hallmark pathways (mh.all.v2002.1.Mm.symbols.gmt) from the MSigDB

365   database were used as inputs for gene set enrichment analysis using the fgsea

366   function from fgsea R package (v.1.22.0) with parameters of eps=0, minSize=5,

367   maxSize =500[36].

368

369

370